Research Article

Kirthika Ramasamy*, Chandrasekar Murugesan, and Senthilkumar Thamilkolunthu

Enhancing the efficiency of polytetrafluoroethylene-modified silica hydrosols coated solar panels by using artificial neural network and response surface methodology

https://doi.org/10.1515/htmp-2022-0273
received June 11, 2022; accepted March 22, 2023

Abstract: In this article, an attempt was made to improve the efficiency of coated solar panels by using artificial neural networks (ANNs) and response surface methodology (RSM). Using the spray coating technique, the glass surface of the photovoltaic solar panel was coated with silicon dioxide nanoparticles incorporated with polytetrafluoroethylene-modified silica sols. Multilayer perceptron with feed-forward back-propagation algorithm was used to develop ANN models for improving the efficiency of the coated solar panels. Out of the 200 sets of data collected, 75% were used for training and 25% were used for testing. On evaluating the models using performance indicators, a four-input technological parameter model (silicon dioxide nanoparticle quantity, coating thickness, surface temperature and solar insolation) with eight neurons in a single hidden layer combination was observed to be the best. The prediction accuracy indicator values of the ANN model were 0.9612 for the coefficient of determination, 0.1971 for the mean absolute percentage error, 0.2317 for the relative root mean square error and 0.00741 for the mean bias error. Using a central composite design model, empirical relationships were developed between input and output responses. The significance of the developed model was ascertained by using analysis of variance, up to a 95% confidence level. For optimization, the RSM was used, and a high efficiency of 17.1% was predicted for the coated solar panel with optimized factors; it was validated to a very high level of predictability. Using interaction and perturbation plots, a ranking of the parameters was done.

Keywords: polytetrafluoroethylene-modified silica hydrosols, anti-reflective coat, solar panel, artificial neural network, analysis of variance, response surface methodology

1 Introduction

In recent times, the energy sector has begun to shift toward solar energy for reducing carbon dioxide emissions [1]. Solar energy is always a clean source of energy and it is available in abundance [2]. Using solar panels, energy from the sun is converted to useful electricity. Solar panels are cost-efficient and are easy to install [3]. Electric power generation using solar panels helps to reduce carbon footprint. Apart from capital expenditure incurred during installation, solar panels can be maintained with very minimal cost. The running cost for a solar power plant is very less compared to other power generation plants [4].

On the other hand, solar panel efficiency (SPE) fluctuates to a large extent as they are installed in an external atmosphere under direct sunlight. They are continuously exposed to dynamic atmospheric conditions involving smoke, dust, rain and snow [5]. The output of a photovoltaic solar panel also depends upon other environmental factors such as solar insolation, air density, rainfall, surface temperature, wind direction and wind speed [6]. Apart from these, shade, dust and dirt accumulation affects the efficiency of solar panels [7].

Anti-reflective coatings (ARCs) on solar panel surfaces help in reducing the amount of light reflected and

* **Corresponding author: Kirthika Ramasamy,** Department of Mechanical Engineering, University College of Engineering, BIT Campus, Anna University, Tiruchirappalli 620024, Tamil Nadu, India, e-mail: kirthikakrishna26@gmail.com, tel: +91 9042112348
Chandrasekar Murugesan: Department of Mechanical Engineering, University College of Engineering, BIT Campus, Anna University, Tiruchirappalli 620024, Tamil Nadu, India, e-mail: shekarpunchu@yahoo.com, tel: +91 9842031537
Senthilkumar Thamilkolunthu: Department of Mechanical Engineering, University College of Engineering, BIT Campus, Anna University, Tiruchirappalli 620024, Tamil Nadu, India, e-mail: kmtsenthil@gmail.com, tel: +91 9443267846

prevent the accumulation of dust with water agglomerations. ARC on the glass surface of the solar panel increases the transmission of solar rays and reduces the wastage of incident sunlight [8]. Even a slight reduction in solar ray reflection results in a 3–5% increase in SPE [9]. ARCs are being prepared by using different materials such as polyelectrolyte-treated SiO_2 [10], MgF_2 [11], Ta_2O_5 [12] and Al_2O_3 [13].

On using SiO_2 nanoparticles as additives in ARCs, a considerable improvement in optical transmittance was observed [14]. Other Ag- and Ti-based nanoparticles exhibit nonlinear optical properties, which are difficult to be controlled during synthesis and the coating process [15]. The nanosize and structure of SiO_2 nanoparticles help in modifying the refractive index of the coated surface, enabling better transmittance [16]. The siloxane bonds of SiO_2 nanoparticles enable structural relaxation. This reduces the porosity of the coatings and improves the coating hardness [17]. The presence of SiO_2 nanoparticles in coatings improves the bonding between the coating material and the glass substrate [18]. SiO_2-incorporated coatings exhibit reduced surface roughness [19].

The preparation of ARCs is a complex and long process [20]. A few of the widely used ARC preparation techniques are plasma treatment [21], electro-spinning [22], phase separation [23], polymer solution casting [24] and the sol–gel method [25]. Out of different ARC preparation techniques, the sol–gel method is an easy and economical process. It is more suitable for mass production, compared to other methods [26]. ARCs prepared using the sol–gel method were found to improve the transmittance of light through glass surfaces [27]. As ARCs are intended to strongly adhere to the surface of the substrate, the differences in the material hardness [28], coefficient of thermal expansion [29] and residual stresses between ARC and the substrate should be considered [30]. The sol–gel method offers better domination over the chemical reactions involved in the synthesis process [31]. On using the sol–gel method for preparing ARCs, the structure and porosity of ARCs can be controlled [32] for better adhesion over glass substrates.

Polytetrafluoroethylene (PTFE)-modified silica hydrosol (PTFE-MSH) coatings exhibit better transmittance of visible rays. They also possess anti-reflective and hydrophobic properties [33]. When PTFE-MSH is coated over glass surfaces, the water contact angle of the substrate undergoes a change. Unwanted clogging of water droplets is minimized, and a considerable improvement in the absorption of solar rays along the surface was observed [34]. PTFE-MSH coatings help in reducing surface reflections and moisture penetration from the environment into the photovoltaic panel [35]. Moreover, they increase the resistance of the surface against abrasion wear and dirt-related surface deterioration [36].

A proper procedure and steps should be followed for applying ARCs on the glass panel surface. The ARC parameters should be controlled properly to obtain a proper and uniform coating. The thickness [37], density and porosity [38] of ARCs directly affect the transmissibility of visible light. Different techniques are being used for depositing ARCs on a substrate. Thermal spraying [39], plasma coating [40], dip coating [41] and spray coating [42] are a few widely used methods for coating. At room temperature, spray coating was found to be better than other coating techniques. Spray coating covers more area and achieves a uniform coating thickness (CT). It is easily available and involves simple procedures [43]. For evaluating the efficiency of the coated solar panels, a number of trial-and-error experiments have to be conducted. As the number of experiments increases, the time, labor and costs also increase [44].

Modern methods like artificial neural networks (ANNs) [45] help in the prediction and approximation to very high accuracies, with a minimum number of experimental trials. ANN prediction techniques have been used in solar systems [46], air-conditioning [47], multi-layer systems for fluid transport [48], photovoltaic solar panels [49] and hybrid energy systems [50]. ANN techniques are used to solve complex problems [51] and for predicting the accurate relationship between non-linear systems [52]. There are different neural networks such as multilayer perceptron (MLP) [53], convolution neural networks (CNNs) [54], recurrent neural networks (RNNs) [55], deep belief networks (DBNs) [56] and restricted Boltzmann machines (RBMs) [57]. The RNN uses data in a sequential manner [58], helping in recognizing spellings and linguistic patterns [59]. Branching-in and branching-out sequential predictions can be efficiently done using RNNs [60]. On using RNNs for analyzing table data, the forecasting accuracy was found to be low [61]. The prediction accuracy of RNNs in evaluating tabular data was lower, compared to the prediction accuracy of MLP [62].

CNNs were found to be very efficient in identifying image patterns and positions [63]; however, they cannot interpret temporal information [64]. On using CNN methods for evaluating nonimage sequences, their prediction accuracy was found to be very low [65]. MLP performs well during input-to-output mapping [66]. For classification-based problems, the MLP method exhibits better accuracy [67]. In MLP, the presence of hidden layers with nodes improves the accuracy of predictions [68], and more layers

with labels can be used for supervising the learning process [69]. RBMs use two layers (input and hidden layers) and use a stacking method of piling one layer over the other for iteration [70]. Hence, it is difficult to improve the prediction accuracy as labels are absent in RBMs [71]. The prediction accuracy of the MLP network, on the other hand, can be increased using labels for supervision [72]. DBNs reconstruct their inputs by using probability and feature identification [73] and are similar to RBM machines in which sequential layer-by-layer training is possible [74]. Compared to DBNs, MLP performs better on working with linearly inseparable data [75]. Generally, the number of hidden layers in MLP is lesser compared to the number of hidden layers in DBNs [76]. Hence, the training time required for MLP models is significantly lower than that required for DBN models [77].

Neural networks in artificial intelligence models improve the ability to learn and establish complex and non-linear relationships [78]. In systems where linear programming is difficult to be implemented, neural networks can give accurate solutions [79]. Even when certain data items get corrupted, the entire system proceeds due to the parallel flow of the sequences [80]. Reprogramming in neural networks is not required as it can determine the process and can be executed in any operating system [81].

Hidden layers in ANN models take inputs and produce a modified output according to the activation function and the weights assigned to the inputs [82]. From the inputs, the obtained data are segregated and transformed into a specific output, according to the user requirements [83]. Hidden layers are used to perform multiple and complex operations quickly, without compromise or loss in the accuracy of the predictions [84]. Relationships between the different independent input variables can be identified by hidden layers as they can imbibe very small details [85]. Hidden layers help in the generalization of the system by increasing the non-linearity [86].

Response surface methodology (RSM) is a statistical and mathematical tool, which is being used for multi-criteria decision making [87]. RSM helps to identify the optimized values of the input process parameters for predicting the desired outputs, with minimum experiments and trials. It helps to optimize a model at a lesser cost.

In RSM, the total number of experiments required for arriving at the optimal solution is lower, compared to other classical techniques [88]. The information obtained from the limited number of experiments is comparatively more than the information obtained from other conventional statistical evaluation techniques such as traveling salesman [89], genetic algorithm [90] and hill climbing algorithm [91]. Using RSM, the development of models and graphical plots can be done quickly and the effect of the important variables on the output responses can be identified [92]. In RSM, both dependent and independent parameters can be fluctuated according to our requirements [93]. In many investigations and experiments, the predictability of RSM was found to be appreciably high [94–96]. In RSM optimization, the effectiveness of the design of experiments, response surface equations and adequacy of the models can be checked [97]. In RSM, there is scope for isolating the interested region for further evaluation [98].

The central composite design (CCD) model [99] and the Box–Behnken design [100] model are the widely used estimation models in real-time problems and applications. The number of design points in the Box–Behnken model is lesser than that in the CCD model. The CCD model uses estimation models with imbedded factorial design or fractional factor designs for analyzing the input variables and output responses. It consists of center points augmented with star points with upper and lower limits for the input parameters [101]. The range of the limits of the process variables depends upon the magnitude of the process. The properties of the model determine the center points and the value of the factorial point [102].

Analysis of variance (ANOVA) is a mathematical technique used for the identification of the significance of any developed model [103]. It signifies the prediction accuracy of the developed empirical equations. The co-relation between the predicted and actual output values can be ascertained. With the use of these mathematical techniques, the performance of solar panels can be increased in an economic manner. Hence, in this investigation, an attempt has been made to enhance the efficiency of photovoltaic solar panels by using ARCs, which were prepared by incorporating SiO_2 nanopowder in PTFE-modified silica hydrosols. Important technological parameters were identified by using ANNs and optimized using RSM.

2 Materials and methods

2.1 Solar panel test kit

An indigenously prepared solar panel test kit (Vinamra Enterprises, Jhotwara, Jaipur) was used in the experiments. The solar panel test kit was installed in the roof top of the Department of Mechanical Engineering, University College of Engineering, Tiruchirappalli, Tamil Nadu, India (latitude, 10.6581°N; longitude, 78.7439°E, 88 m approx.

above sea level). A digital temperature sensor (Evelta – 12 C – MRS-P1) was used for measuring the temperature near the surface of the solar panel. The humidity measurement equipment was used to measure the atmospheric humidity near the solar panel. A digital anemometer (Model-WS-102, Logics Power, Delhi, India) was used for recording the wind speed and wind direction. A solar irradiation sensor (Sims Instrumentation, Bengaluru) was used for measuring the solar irradiation on the surface of the panel. For measuring precipitation, a tipping rain gauge sensor (Balaji Hydromet, Roorkee, Haridwar, India) was used. Using indigenously fabricated module mounting structures, the solar panel was placed on the terrace away from the shade. Dust cleaners and air blowers were used for cleaning the solar panels before starting the experiments and while taking readings. A digital multi-meter (HTC BM) was used for measuring the open circuit voltage (mV) and short circuit current (mA).

2.2 ARC preparation

The following chemicals were used for preparing antireflective PTFE-modified silica hydrosols. Soda lime heat-resistant glass sheets (1.35 mm thick) were bought from Akshar Exim Company Private Limited (West Bengal, India; 99% pure). Ammonium hydroxide and PTFE were purchased from Ecokem Technologies Private Limited (Navi Mumbai, India; 99% pure). Tetraethyl orthosilicate was bought from Tritech Catalyst & Intermediate (Pune; 99.9% pure). Silicon dioxide nanopowder and 98% pure hexamethyldisiloxane (HMDS) were bought from Supreme Silicones (Maharashtra, India); and 99.9% pure ethanol and de-ionized water were purchased from Sigma Aldrich Chemicals (Bangalore, India).

By using the Stober method [104], the precursor solution for silica sol was prepared. Tetraethyl orthosilicate/ethanol/ammonium hydroxide/de-ionized were mixed in a molar ratio of 1:0.17:38:0.17. The mixture was stirred using a magnetic stirrer at 25°C for 3 h. Then, the mixture was transferred into a clean airtight glass container and stored in a dark place for 1 week. After 1 week, PTFE was added to it and stirred for 3 h using a magnetic stirrer at 25°C. Again, the solution was sealed airtight and stored in a cool and dark place for 1 week [105]. Then, the SiO_2 nanopowder was mixed with the solution (at 750 mg to 1 g per 1,000 ml solution). The mixture was agitated using ultrasonication. SiO_2 nanoparticles were added to improve water repellence and transmittance [106].

2.3 Glass surface preparation and spray coating

The glass substrate placed on the solar panel surface was cleaned with de-ionized water, acetone and hydrochloric acid. This three-step cleaning process was to ensure proper adhesion of the coating material to the substrate. The glass sheets were immersed in ethanol and prior to spray coating, they were heated to 80°C in an electrical portable furnace. The PTFE-modified silica hydrosol solution with SiO_2 nanoparticles was applied on the glass surface using the spraying equipment (Gautham Kit, Haryana). The diameter of the spraying nozzle was 1.25 mm, and spraying was done at 40 psi pressure. The distance between the spraying equipment and the substrate was maintained at 100 mm for all coatings. After spraying, the glass substrate was allowed to dry in a portable furnace at 80°C for 10 min. A 75–90 nm-thick coating was obtained after a single spray coat. The thickness of the coatings was measured by using a nanocoat meter (Presice-UTM09), with an accuracy of ±5 nm. The coat meter was calibrated with standard nanofilms prior to the actual measurement. This process was repeated till the desired thickness of the coating was attained on the glass. Before using the glass on the solar panel, it was immersed in HMDS solution for 2 days and dried. This was done to enhance the hydrophobic characteristics of the coating [107]. The solar panel test setup is shown in Figure 1.

The efficiency of the solar panel was calculated using the following formula:

$$\eta = \frac{\text{Output power}}{\text{Input power}} = \frac{P_{\max}}{P_{\text{inp}}}, \tag{1}$$

$$P_{\max} = V_{\max} \times I_{\max}, \tag{2}$$

$$P_{\text{inp}} = \text{Input solar irradiance} \times \text{Area of the solar cell}. \tag{3}$$

In the aforementioned equations, η is the efficiency of the solar panel, $P_{\max}$ is the maximum power of the solar panel, P_{inp} is the power generated in the solar panel, $V_{\max}$ is the maximum voltage of the solar panel and $I_{\max}$ is the maximum current of the solar panel

2.4 Developing ANN models using MLP

In this investigation, ANN models were developed with important coating parameters and photovoltaic solar panel input parameters. The coating parameters considered in the experiments were the SiO_2 nanoparticle quantity in $mg{\cdot}l^{-1}$ (SNP), the spraying pressure in psi (SP),

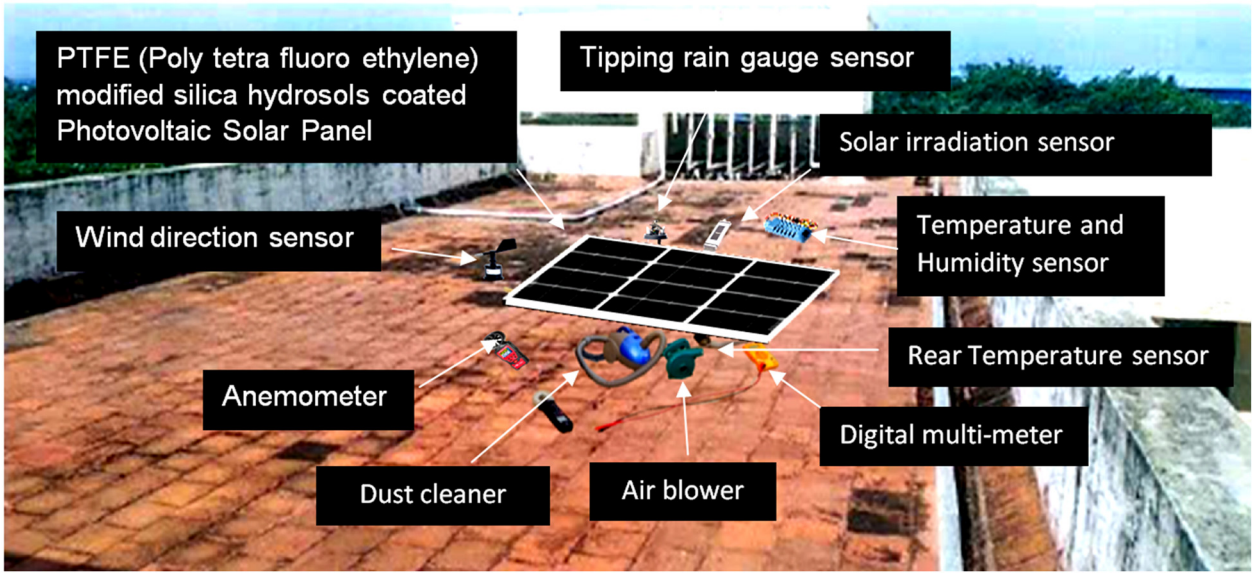

Figure 1: Solar panel test kit used for conducting the experiments.

the CT in nm, the spraying distance in mm (SpD), the drying duration in a furnace in min (DD), the furnace temperature in °C (FT) and the nozzle spray diameter in mm (ND) [108].

The photovoltaic solar panel input parameters considered in the experiments were the mean relative humidity in % (MRH), the square temperature in °C (ST), the daily maximum temperature in °C (DT_{max}), the daily minimum temperature in °C (DT_{min}), solar irradiation at the panel surface in $W{\cdot}h{\cdot}m^{-2}$ (SIS), wind velocity in $m{\cdot}s^{-1}$ (WV), the wind direction in degrees (°) (WD), the difference between the daily maximum and minimum temperature in °C ($\Delta T_{max\text{-}min}$), daily precipitation in mm (DPp), daily maximum relative humidity in % (D_{max}RH), daily minimum relative humidity in % (D_{min}RH) and solar altitude angle in ° (SAA) [109]. During the selection of the input variables, the average performance for ten runs was taken for the input variables. This was done to avoid random measurement errors and to increase the reliability of the developed ANN model [110].

Initially, the ANN model was developed based on the coating and solar panel input technological parameters. Then, the relevance of the individual and combined technological parameters was studied. An incremental method was used for identifying the feasible combination of the input technological parameters. For the identification of the best model, testing was done using different numbers of neurons in a single hidden layer [111]. The important technological parameters affecting the output efficiency of the solar panel were identified. Data collection was done for 3 months, preferably in the afternoon time in a clear sky. A total of 200 data sets were collected. Out of the data sets collected, 75% were used for training and 25% were used for testing. The values of the data sets collected for the investigation are shown in Figure 2.

Out of different neural networks, such as MLPs, CNN, RNN, DBN and RBM, in this investigation, the MLP network was used. As the number of input parameters was more, probability-based predictions were required. As the MLP can be used to predict accurate solutions in complex non-linear problems in a very short time after training [112], it was used in this investigation. The data were handled by a feed-forward neural network in two stages. The training process was the first stage. In this process, ANN weights were adjusted to match the input group. In the second stage, the generalization of the network was done to match the training data [113]. With this, the prediction was done. The learning process was continued by training the data and updating the weights of the data till the desired goal was achieved. The Levenberg–Marquardt feed-forward back-propagation training algorithm with a single hidden layer was used for developing the ANN models [114]. The MLP with one input, one output and one hidden layer is shown in Figure 3.

The input to the hidden layer was sent through the input layer. The output of the first layer was the summation of inputs multiplied by their corresponding weights. The output of the first layer is shown in the following equation:

$$Y_i = \int \left(\sum w_i x_i \right), \tag{4}$$

where x_i is the input signal, w_i is the weight of the input and Y_i is the output of the first layer. The Levenberg–Marquard

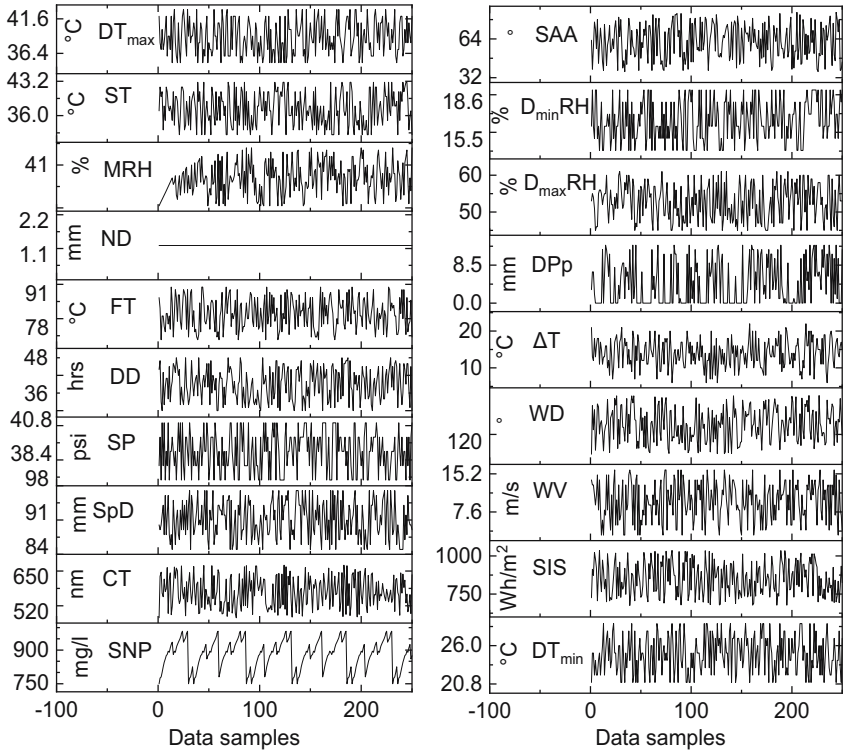

Figure 2: Values of the data collected for this investigation.

backpropagation algorithm with a gradient descent method was used for updating the weights during the learning algorithm [115]. Learning rule training algorithms with supervised learning were used for the ANN models [116]. Out of 200 datasets collected, 75% (150 data sets) were used for training and 25% (50 datasets) were used for testing.

Using a single hidden layer, several runs for each combination of input and hidden neurons were conducted. In the hidden and output layers, hyperbolic tangent and linear functions were used as activation functions [117].

The hyperbolic activation function equation is as follows:

$$f(x) = \tanh(x) = \frac{(e^{x} - e^{-x})}{(e^{x} + e^{-x})} = \frac{2}{1 + e^{-2x}} - 1. \quad (5)$$

The linear activation function equation is as follows:

$$f(x) = w^{T}x + b. \quad (6)$$

In the above equations, x is the input, w is the weight and b is the bias [118].

Four prediction accuracy indices were used for identifying the prediction of the ANN model [119]. They were

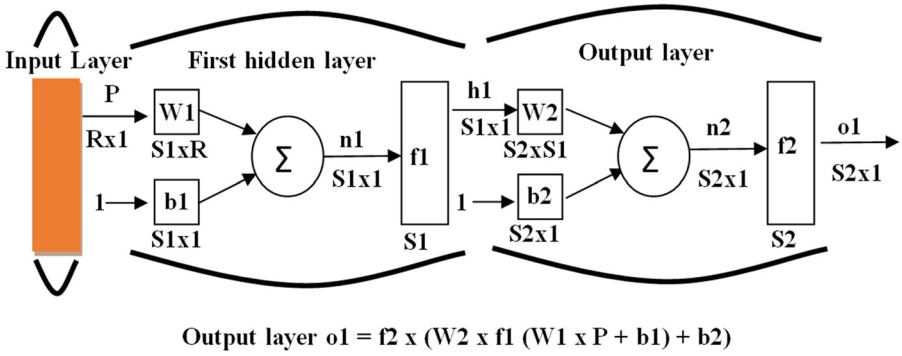

Figure 3: The MLP with one input, one output, and one hidden layer.

the mean absolute percentage error (MAPE) [120], the relative root mean square error (RRMSE) [121], the coefficient of determination (R^2) [122] and the mean bias error (MBE) [123].

For the evaluation of forecasting accuracy, MAPE is used. MAPE indicates the percentage of deviation from the actual output [124]:

$$\text{MAPE} = \frac{1}{n}\sum_{t=1}^{n}\frac{\text{ADV}_t - \text{FDV}_t}{A_t}, \tag{7}$$

where ADV_t denotes the actual data value, FDV_t denotes the forecasted data value and n is the number of true values.

The coefficient of determination (R^2) is used for the prediction of future outcomes. For independent variables, R^2 is ascertained by using variance proportion [125]:

$$y' = \frac{1}{n}\sum_{i=1}^{n} y_i, \tag{8}$$

where y' is the mean of the dataset y_i and n is the number of values in the dataset y_i. The total sum of squares (SST) is defined as follows [126]:

$$\text{SST} = \sum_{i=1}^{n}(y_i - y')^2. \tag{9}$$

The error sum of squares (SSE) is defined as follows [127]:

$$\text{SSE} = \sum_{i=1}^{n}(y_i - f_i)^2. \tag{10}$$

where f_i is the predicted data value

The SSE and SST are used to determine the R^2 value as follows [128]:

$$R^2 = 1 - \frac{\text{SSE}}{\text{SST}}. \tag{11}$$

R^2 is used for identifying the proximity of the predicted data to the regression line, and its value varies from 0 to 100%. 0% indicates that not even a single predicted data was close to the regression line of fit, and 100% indicates that all the predicted data were close to the mean.

The RRMSE is used for measuring the average value of the errors, and is defined as follows [129]:

$$\text{RRMSE} = \sqrt{\frac{1}{n}\sum_{i=1}^{n}(Y_i - X_i)^2}, \tag{12}$$

where Y_i and X_i are the n numbers of predicted and true data. Low values of RRMSE indicate that the deviation between the regression fitted data line and the predicted data is less, and high values of RRMSE indicate that the deviation from the mean is higher.

MBE is the average of the prediction error [130]. It is a systematic error, which indicates underprediction or overprediction of a developed model, and is defined as follows:

$$\text{MBE} = \frac{1}{n}\sum_{i=1}^{n}(Y_i - X_i). \tag{13}$$

Using these performance indicators, the relevance of each technological input parameter was assessed. Using the incremental method [131], the relevant input technological parameters were progressively added and their effect on the prediction model was studied [132].

As the MLP incorporates the universal approximation theorem, the approximation of the obtained values close to the desired output can be achieved with one hidden layer [133]. As the number of input parameters was large and a progressive method was adopted to add and substitute the technological parameters, MLP with one hidden layer was chosen for this investigation.

Different incremental combinations were studied, and the best combination of technological parameters was identified. The identified combination was tested using different neurons within a single hidden layer. The number of neurons in a single hidden layer, which exhibited the best prediction accuracy indices, was identified.

2.5 Developing empirical relationships and optimization using RSM

The feasible limits of important input technological parameters were identified by using trial experiments. The CCD model with six stars, six central and eight design points was selected. The number of input factors considered was 3, and the range of the parameters was 5. Even though the number of design points in the Box–Behnken design model was low, the CCD model was chosen to reduce errors and improve estimation accuracy. Using the CCD model, 20 different combinations of technological parameters were developed [134]. With each combination of the input technological parameter values, experiments were conducted and the output (SPE) was recorded. Out of the 20 different combinations, 14 were unique and 6 were repetitive experiments. The repetitive experiments were used for reducing the errors during the experimentation process.

Using the second-order regression equation [135], empirical relationships were developed between the technological input parameters and the output (panel efficiency). The relationship and closeness between the predicted and actual output values were studied. Using ANOVA, the

significance of the developed model was ascertained [136]. In this investigation, a two-way- partial sum of squares-type III ANOVA technique was used to identify the significance of the developed model. It was used for identifying the significance of the developed model. It signifies the predictability and accuracy of the developed empirical relationship between the input technological parameters and the output SPE. RSM was used for optimizing important technological parameters. It was chosen as it is an easy and economical method to identify the optimized output, with a minimum number of inputs [137]. Contours [138] and surface plots [139] were developed to identify the optimum values of the input technological parameters for achieving highest possible efficiency. The developed model was validated by using validation experiments to identify the predictability of the optimization model. Using interaction [140] and perturbation [141] plots, ranking of the technological parameters was done.

3 Results and discussion

3.1 ANN analysis

The performances of the individual technological parameters of the solar panel setup were evaluated by using the MLP ANN technique. With the Levenberg–Marquardt feed-forward back-propagation training algorithm, MAPE, RRMSE, MBE and R^2 values of SNP, CT, SpD, SP, DD, FT, ND, MRH, ST, DT_{max}, DT_{min}, SIS, WV, WD, $\Delta T_{max\text{-}min}$, DPp, $D_{max}RH$, $D_{min}RH$ and SAA were calculated. The values of the performance indicators for the input variables are shown in Table 1.

From Table 1, the input technological process parameters exhibiting higher performance indicator values were identified. This was used to identify the input technological process parameters into parameters of primary, secondary and tertiary importance. Depending upon the value of R^2, MAPE, RRMSE and MBE, SNP, CT, SpD, SP, MRH and SIS were identified as primary process parameters. For identifying the effect of individual technological parameters, the inputs were incrementally combined [142]. Priority was given to the addition and substitution of primary technological process parameters, as their inclusion and removal affected the values of overall prediction accuracy indices.

The secondary parameters such as DD, FT, ND, WV and WD were included in the incremental combination model if there was an improvement in the overall average performance indices. Tertiary parameters such as DPp, $D_{max}RH$, $D_{min}RH$, SAA and $\Delta T_{max\text{-}min}$ were removed and substituted with another technological parameter, as they did not contribute for improving the performance indices.

Table 1: Performance indicator values for individual technological parameters

Sl. No.	Input variables	Units	Abbreviation	Performance indicator values			
				MAPE (%)	RRMSE (%)	MBE (%)	R^2 (%)
1	SiO_2 nanoparticles	$mg{\cdot}l^{-1}$	SNP	41.84	30.47	2.05	89.96
2	Coating thickness	nm	CT	37.35	28.32	1.98	91.38
3	Spraying distance	mm	SpD	66.41	43.54	2.46	84.65
4	Spraying pressure	psi	SP	37.45	29.05	−0.51	86.39
5	Drying duration	h	DD	29.45	40.21	2.36	73.29
6	Furnace temperature	°C	FT	32.19	25.96	1.90	82.15
7	Nozzle diameter	mm	ND	56.14	31.44	2.09	89.21
8	Mean relative humidity	%	MRH	81.21	32.41	2.12	90.17
9	Square temperature	°C	ST	43.61	34.61	2.19	89.78
10	Daily maximum temperature	°C	DT_{max}	39.34	29.63	−1.03	90.83
11	Daily minimum temperature	°C	DT_{min}	62.54	33.65	2.16	81.08
12	Solar irradiation at the panel surface	$W{\cdot}h{\cdot}m^{-2}$	SIS	48.59	26.84	1.93	92.17
13	Wind velocity	$m{\cdot}s^{-1}$	WV	23.89	28.44	−0.98	79.86
14	Wind direction	deg	WD	57.32	32.14	2.11	78.42
15	Difference $DT_{max} - DT_{min}$	°C	$\Delta T_{max\text{-}min}$	46.22	31.91	2.10	72.86
16	Daily precipitation	mm	DPp	32.74	43.12	−1.45	76.62
17	Daily maximum relative humidity	%	$D_{max}RH$	36.45	36.41	2.25	88.43
18	Daily minimum relative humidity	%	$D_{min}RH$	38.54	32.66	2.13	87.11
19	Solar altitude angle	deg	SAA	52.13	41.84	2.41	86.82

Table 2: Average performance of the progressive incremental combinations

Sl No.	Input variables	Performance indicator values			
		MAPE (%)	**RRMSE** (%)	**MBE** (%)	R^2 (%)
1	SNP, CT	32.12	23.64	0.981	93.41
2	SNP, CT, SIS	31.21	23.82	0.9833	92.06
3	SNP, CT, SIS, D_{max}RH	27.65	23.14	0.972	92.87
4	SNP, CT, SIS, SAA, D_{min}RH	27.41	24.39	0.996	92.16
5	SNP,CT, SIS, D_{max}, RH, DT_{max}	33.54	25.45	1.016	92.66
6	SNP,CT, SIS, D_{max}, SP, DT_{min}	32.84	26.12	1.034	92.93
7	SNP, CT, SIS, D_{max}, RH, WV	29.23	25.21	1.013	91.02
8	SNP, CT, SIS, D_{max}, RH, WD	28.78	27.23	1.053	90.14
9	SNP, CT, SIS, D_{max}, RH, DpT	30.51	26.21	1.033	90.02
10	SNP, CT, SIS, D_{max}, RH, MRH	31.12	27.14	1.051	90.21

Progressively, ten combinations of input parameters were developed and their average performances were recorded. The performance of the progressive incremental combination models is shown in Table 2.

From Table 2, it is observed that the individual performance of the input parameters does not improve the global performance of the model. Increasing the number of input technological parameters does not contribute to improving the performance of the developed ANN model [143]. Comparable performance was observed for a combination with two input parameters in the first model and a combination with five input parameters in the sixth model.

Investigations have shown enhanced statistical performance for a combination of input parameters having lower individual performance [144–146]. Experimental tests were conducted to explore other combination possibilities even with input parameters having lower individual performances. For test data of ten runs, the average statistical performance indicator values for different combinations of lower individual performance exhibiting parameters are shown in Table 3.

The combinations are listed in decreasing order of the performance indicator values. It was observed that the input combination of SiO_2 nanoparticles addition, CT, daily maximum surface temperature and solar insolation at the panel

Table 3: Average performance indicators for different input combinations

Sl No.	Combinations	Performance indicator values			
		MAPE (%)	**RRMSE** (%)	**MBE** (%)	R^2 (%)
1	SNP, CT, DT_{max}, SIS	22.31	18.74	0.813	95.78
2	CT, DT_{max}, MRH	22.42	18.93	0.816	95.61
3	CT, DT_{max}	22.69	19.14	0.823	94.87
4	ND, DPp, SNP	22.93	19.27	0.826	94.59
5	DT_{max}, WV, DPp	23.12	19.56	0.831	94.41
6	D_{max}, RH, ND, SIS	23.44	19.78	0.836	94.18
7	ST, ND, RH, SP	23.84	19.62	0.833	93.85
8	FT, DT_{min}, ST	24.12	19.84	0.836	93.63
9	CT, DT_{max}, WV, SAA	24.39	20.12	0.843	93.57
10	SAA, D_{min}, SNP	24.68	20.45	0.851	93.33
11	$\Delta T_{max\text{-}min}$, MRH, SIS, DD	24.83	20.68	0.853	93.18
12	SIS, SpD, FT	25.12	20.81	0.856	92.89
13	MRH, SAA	25.34	21.12	0.863	92.74
14	FT, DT_{min}	25.26	20.93	0.862	92.69
15	CT, DPp, SpD	25.37	21.24	0.866	92.58
16	$\Delta T_{max\text{-}min}$, WD, ND	25.42	21.38	0.874	92.43
17	$\Delta T_{max\text{-}min}$, SAA	25.63	21.47	0.872	92.34
18	SNP, WV, FT	25.81	21.53	0.873	92.29

Table 4: Average performance indicators for the best combination of increasing the number of neurons from 1 to 20

No. of neurons	Performance indicator values			
	MAPE (%)	RRMSE (%)	MBE (%)	R^2 (%)
1	19.86	23.46	0.786	95.67
2	18.76	22.12	0.763	95.85
3	19.46	23.13	0.781	95.67
4	18.72	21.97	0.764	95.89
5	19.54	23.74	0.795	95.52
6	19.85	22.79	0.773	95.68
7	21.65	23.74	0.794	95.68
8	18.65	21.83	0.756	95.94
9	21.74	23.81	0.793	95.64
10	19.77	23.54	0.786	95.69
11	18.79	22.17	0.763	95.79
12	18.73	21.99	0.764	95.86
13	19.64	23.41	0.768	95.72
14	19.41	22.26	0.775	95.74
15	21.45	23.65	0.772	95.65
16	18.81	22.21	0.781	95.78
17	19.81	22.45	0.784	95.71
18	19.23	22.47	0.778	95.75
19	18.95	22.24	0.776	95.77
20	21.22	23.48	0.774	95.64

surface was the best with MAPE = 22.31%, RRMSE = 18.74%, MBE = 0.813% and R^2 = 95.78%.

The best combination of input parameters was tested with different numbers of neurons in the hidden layer. By increasing the number of neurons from 1 to 20, the average performance indicator values for the best (SNP, CT, DT_{max}, SIS) model were evaluated and shown in Table 4. The best architecture was obtained with eight neurons, with R^2 = 95.94%, MAPE = 18.65%, MBE = 0.756% and RRMSE = 21.83%. The correlation between the predicted and the actual efficiency of the PV solar panel is shown in Figure 4.

The estimated values of the selected model with eight neurons in the hidden layer versus the actual efficiency of the training dataset are shown in Figure 4(a), and that for the test dataset is shown in Figure 4(b). A good level of agreement is observed between the predicted and measured efficiencies. The selected configuration exhibited average performance indicator values of R^2 = 96.12%, RRMSE = 23.17%, MBE = 0.741% and MAPE = 19.71%.

Using ANN, a reliable estimation model was obtained to predict the efficiency of the solar panel using technological parameters such as the SiO_2 nanoparticle quantity, thickness of the PFTE-modified silica hydrosols CT, temperature and solar irradiance. The reliability of the present model has been evaluated with the prediction parameter values of the models developed in previous investigations. The present investigation, using the incremental method

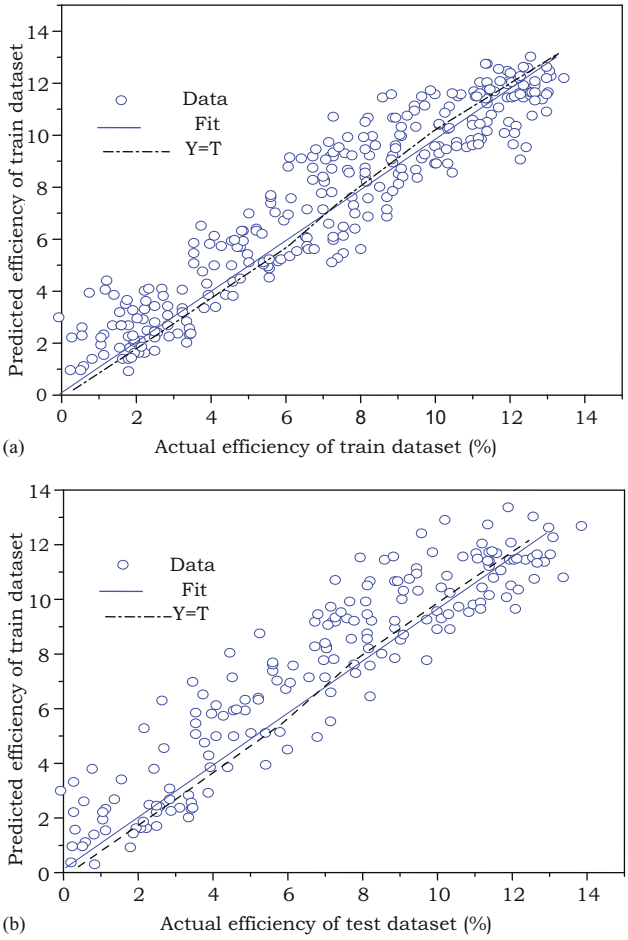

Figure 4: Estimated and actual SPEs of the (a) training dataset and (b) testing dataset.

for ANN, was compared with the accuracy results of other solar models of related research works. The comparison is shown in Table 5. In comparison, the present model was found to exhibit better performance indicator values for the ANN models developed [147–156].

3.2 Identification of feasible limits of technological parameters

Out of the 19 different technological parameters of the solar panel model, 3 important technological parameters were selected as the primary parameters for further evaluation. The experiments were *conducted in a clear sky* and between 1:30 to 3:00 PM when the solar irradiance was highest. At peak days, the solar irradiation was around 1,000 $W{\cdot}m^{-2}$ (approx., 985–1,015 $W{\cdot}m^{-2}$). The output of the solar panel was measured when the solar irradiation was around 1,000 $W{\cdot}m^{-2}$. The presence of ARC caused a significant improvement in the solar panel output efficiency. On

Table 5: Comparison of the present incremental method with other related research works

Sl. No.	Literature reference	ANN method	Performance indicator values (absolute)			
			MAPE	RRMSE	MBE	R^2
1	Present research	MLP	**0.1971**	**0.2317**	**0.00741**	**0.9612**
3	Khatib et al. [147]	MLP	0.592	7.96	0.0146	—
4	Salima and Cahvula [148]	Linear regression	—	1.72	0.015	0.9
5	Assi et al. [149]	MLP and radial basis function	—	0.27	0.008	0.9212
6	Yacef et al. [150]	Bayesian neural network	—	1.318	0.2526	0.8074
7	El-Sebaii et al. [151]	Liu and Jordan's isotropic model and Klucher's anisotropic model	—	0.044	0.015	0.92
7	Poudyal et al. [152]	Modified Angstrom model	—	0.071	0.055	0.71
8	Tuomiranta et al. [153]	Thermal model	—	4.8	—	0.958
9	Bimenyimana et al. [154]	Nonlinear autoregressive neural network	—	—	—	0.736
10	Yaniktepe and Genc [155]	Statistical model	1.5943	0.083	—	—
11	Kumar and Kaur [156]	MLP	0.1645	—	—	0.8841

To emphasize that the values were calculated in this experimental investigation, it is given in bold.

conducting experimental trials, a 3.1–3.6% increase in the output efficiency was observed, compared to the uncoated solar panels. From previous investigations and trial experiments, the other technological parameters were fixed as constant. For all coating experiments, the distance between the spraying nozzle and substrate was fixed at 100 mm [157], the nozzle diameter as 1.25 mm [158], the spraying pressure as 40 psi [159], the drying duration as 10 min [160] and furnace temperature as 80°C [161]. PFTE-treated silica sol coating was used to improve the transmissibility of solar rays. SiO_2 nanoparticles were added to improve the hydrophobic nature of the coatings. Temperature also plays an important role. Even though the ARC improved the efficiency of the solar panel, operating the solar panels at optimum temperatures caused further improvement in the SPE. Experimental trials were conducted with different CTs, quantity of SiO_2 nanoparticles and surface temperatures. Using blowers and cooling panels, the temperature was reduced and readings were taken.

a. Trials conducted using CT lesser than 200 nm did not help in improving the efficiency of the solar panel.
b. Coatings with thicknesses greater than 800 nm were costly. Thick coatings created coating surface discrepancies and reduced the efficiency of the solar panel.
c. Addition of SiO_2 nanopowder lesser than 750 mg·l^{-1} to the coating solution did not improve the water repulsion characteristics of the solar panel. Repulsive rolling of dew drops from the panel did not occur.
d. Addition of SiO_2 nanopowder of more than 1,500 mg·l^{-1} caused undesirable surface roughness. The transmittance of solar rays and the efficiency of the solar panel are reduced.
e. At temperatures lower than 20°C, due to the formation of mist and dew drops, dust accumulation occurred. As the temperature in South India would peak to 40°C, the efficiency of the panels was recorded at 45°C.
f. Operating the solar panel beyond 45°C caused a reduction in efficiency.

Thus, within a CT of 200–800 nm, the SiO_2 nanopowder quantity within 750–1,500 mg·l^{-1} and surface temperatures within 20–45°C were identified to be feasible.

3.3 Central composite matrix development

The feasible parameters, such as the CT in nm, the SiO_2 nanoparticle quantity in mg·l^{-1} (SNP) and the temperature at the panel surface in °C (T), were used for further

Table 6: Feasible limits and intermediate values of the technological parameters

No.	Parameters	Notation	Unit	Level				
				−1.682	**−1.0**	**0**	**+1.0**	**+1.682**
1	Coating thickness	CT	nm	200	320	500	680	800
2	SiO_2 nanoparticle quantity	SNP	mg·l^{-1}	750	900	1,125	13,450	1,500
3	Temperature at the panel surface	T	°C	20	25	32.50	40	45

evaluation. The feasible limits of the technological parameters are shown in Table 6.

A CCD model with three factors and five levels (–1.68, –1, 0, +1, +1.68) was chosen, as the range of the individual factors was large. A second-order quadratic model can be established with a minimum number of experiments using CCD. In this experimental investigation, three factors (coating thickness [CT], SiO_2 nanoparticles quantity [SNP] and temperature of the solar panel [T]) were chosen to improve one response (SPE). Hence, for developing the CCD model, six center points and one axial point were chosen. This was done to improve the accuracy of the predictions in RSM. The design model was developed with six stars and center points. Using CCD, 20 sets of process parameter conditions were developed according to the procedure developed by Montgomery [162].

A value of +1.682 was coded as the upper limit and –1.682 was coded as the lower limit. Using the relationship developed by Montgomery [162], the intermediate values were calculated as follows:

$$J_i = 1.\ 682[2J - (J_{\max} + J_{\min})] \div (J_{\max} + J_{\min}). \quad (14)$$

In equation (14), the coded value of J is J_i. J is made to take any value from $J_{\max}$ to $J_{\min}$. The maximum value for a variable is denoted as $J_{\max}$ and the least value of a variable is denoted as $J_{\min}$. The intermediate values are shown in Table 5. The CCD model developed with 20 different combinations of technological process parameters is shown in Table 7.

With the technological parameter values indicated in the design model, 20 experiments were conducted. With an appropriate SiO_2 nanoparticle addition, CT and temperature, the output of the solar panel was measured. The efficiency was evaluated and their values are indicated in Table 7. Out of the 20 different experimental combinations developed in the CCD model, 14 experiments were distinct and 6 experiments (3rd, 9th, 12th, 14th, 17th and 19th) were repetitive. These repetitive experiments were used for reducing the errors that arise during the experimentation process. The standard error of the design is shown in Figure 5.

3.4 Establishing empirical relationships between the technological parameters and output efficiency

The responses (efficiency of the solar panel) are attributed to be a function of the three technological parameters such as the CT (in nm), SiO_2 nanoparticle quantity (SNP in $mg{\cdot}l^{-1}$) and temperature of the panel surface (T in °C). As per the methodology developed by Paventhan et al. [163], the relationship between the input variables and output responses is shown in the following equation:

Table 7: CCD model with responses

Sl. No.	Coded factor value			Actual factor value			Responses (SPE)
	CT	SNP	T	CT (nm)	SNP ($mg{\cdot}l^{-1}$)	T (°C)	Solar panel η (%)
1	+1	–1	–1	680	900	25.0	15.6048
2	–1.68	0	0	200	1,125	32.5	15.8243
3	0	0	0	500	1,125	32.5	16.5028
4	–1	+1	+1	320	1,350	40.0	16.2633
5	+1	+1	+1	680	1,350	40.0	16.0838
6	–1	–1	+1	320	900	40.0	15.8044
7	0	0	+1.68	500	1,125	45.0	16.4829
8	+1	–1	+1	680	900	40.0	17.1015
9	0	0	0	500	1,125	32.5	16.5627
10	+1	+1	–1	680	1,350	25.0	15.8243
11	0	0	–1.68	500	1,125	20.0	15.3654
12	0	0	0	500	1,125	32.5	16.5826
13	+1.68	0	0	800	1,125	32.5	16.423
14	0	0	0	500	1,125	32.5	16.6225
15	0	–1.68	0	500	750	32.5	15.7046
16	0	+1.68	0	500	1,500	32.5	16.2633
17	0	0	0	500	1,125	32.5	16.5826
18	–1	+1	–1	320	1,350	25.0	16.403
19	0	0	0	500	1,125	32.5	16.6026
20	–1	–1	–1	320	900	25.0	14.627

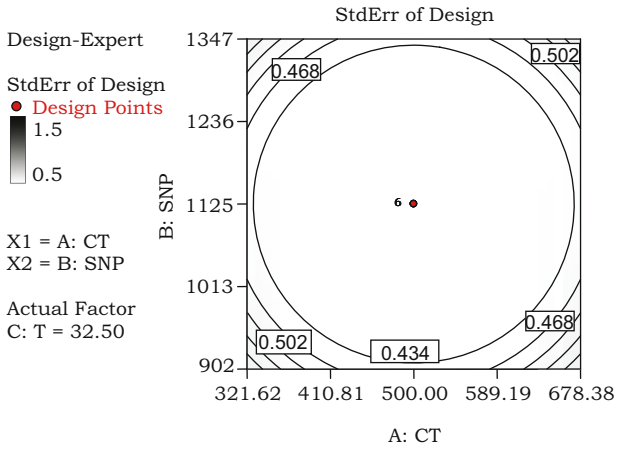

Figure 5: Standard error of the design.

$$\text{SPE} = f(\text{CT}, \text{SNP}, T). \tag{15}$$

Using a second-order polynomial regression equation [164], the response surface Q of the solar panel model is given as

$$Q = n_0 + \sum n_i x_i + \sum n_{i1} x_{i2} + \sum n_{ij} x_i x_j. \tag{16}$$

For the three input variables, such as the CT (nm), SiO_2 nanoparticles quantity (SNP) (mg·l^{-1}) and temperature (T) of the panel surface (°C), the second-order polynomial equation is represented as follows:

$$\begin{aligned}\text{SPE} = \{&n_0 + n_1(\text{CT}) + n_2(\text{SNP}) + n_3(T)\\ &+ n_{12}(\text{CT} \times \text{SNP}) + n_{13}(\text{CT} \times T)\\ &+ n_{23}(\text{SNP} \times T) + n_{11}\text{CT}^2 + n_{22}\text{SNP}^2 + n_{33}T^2\}.\end{aligned} \tag{17}$$

In the above equations, n_0 is the average of the responses and n_1, n_2, n_3,..., are the coefficients of the regression equations. These depend upon the linear terms, interaction terms and squared terms of the input technological parameters [165]. These coefficients were evaluated by using Design Expert Software. Student's t-tests were used for the evaluation of the individual coefficients and their significance was identified using p values [166]. Using the partial sum of squares-type III ANOVA (ANOVA) technique, the significance of the developed model was ascertained. The ANOVA results of the solar panel model are shown in Table 8. Using ANOVA, the sum of squares, mean square, F-ratio and p-values for Model, CT, SNP, T, CT × SNP, CT × T, SNP × T, CT^2, SNP^2 and T^2 were evaluated. The F-ratio value of the developed model was found to be 566.78. From this value of the F-ratio, it was inferred that the model was significant. The chance for the occurrence of this large value of F-ratio was only 0.01%. In the developed model, the "lack of fit" value was 0.39. It indicated that "lack of fit" was not significant w.r.t., pure error of the model. The chance for the occurrence of this large lack of fit value was found to be 84.09%. "Prob > F" values for Model, CT, SNP, T, CT × SNP, CT × T, SNP × T, CT^2, SNP^2 and T^2 were found to be <0.0001. "Prob > F," lesser than <0.0500, is a clear indication that the developed model was significant at the 95% confidence level. When Prob > F values are greater than 0.10, the model terms were termed insignificant. From ANOVA, as Prob > F values for the model, individual parameters, product of the two parameters and square of the parameters were lesser than 0.0500, the model was attributed to be significant up to a confidence level of 95%.

The developed empirical relationship for the solar panel model is given as follows:

Table 8: ANOVA test results of the solar panel model

Source	Sum of squares (SS)	Degree of freedom (df)	Mean square (MS)	F-ratio	p-value Prob >F	Note
Model	6.03	9	0.67	566.78	<0.0001	Significant
CT	0.47	1	0.47	396.39	<0.0001	
SNP	0.41	1	0.41	353.21	<0.0001	
T	1.60	1	1.6	1356.14	<0.0001	
CT × SNP	1.17	1	1.17	977.74	<0.0001	
CT × T	0.065	1	0.065	54.76	<0.0001	
SNP × T	0.82	1	0.82	693.18	<0.0001	
CT^2	0.38	1	0.38	324.49	<0.0001	
SNP^2	0.65	1	0.65	548.49	<0.0001	
T^2	0.78	1	0.78	664.73	<0.0001	
Residual	0.012	10	1.17×10^{-3}			
Lack of fit	3.2×10^{-3}	5	6.5×10^{-4}	0.39	0.8409	Not significant
Std. Dev		0.034		R^2	0.9981	
Mean		16.16		Adj	0.9963	
CV %		0.21		Pred	0.9936	
Press		0.038		Adeq precision	101.002	

$$\begin{aligned} \text{SPE} = \{&16.58 + 0.18(\text{CT}) + 0.17(\text{SNP}) + 0.34(T) \\ &- 0.38(\text{CT} \times \text{SNP}) + 0.090(\text{CT} \times T) \\ &- 0.32(\text{SNP} \times T) - 0.16\text{CT}^2 - 0.21\text{SNP}^2 \\ &- 0.23T^2\}. \end{aligned} \tag{18}$$

The adequacy of the developed solar panel model was verified from the response surface model of the second order. R^2 is the coefficient of determination. The goodness of fit of the model is identified by using the value of R^2. From Table 8, the R^2 value (0.9981) indicated that the very minimal extent of variations was not explained [167]. The adjusted R^2 (0.9963) value was found to be very high. It indicated that the level of significance of the developed model was high. A good level of agreement was observed between the adjusted coefficient of determination value and the predicted R^2 value. As the value of the determination coefficient was greater than 0.95, a high level of correlation between the predicted SPE and the measured SPE was observed. The scatter diagram indicating the correlation between the predicted and actual SPE is shown in Figure 6. From the scatter diagram, a very close relation between the predicted and actual efficiency is observed.

3.5 Optimization of the technological parameters and validation

Using RSM, the three technological parameters were optimized to increase the SPE to the maximum possible extent. A functional relationship was established between the independent variables such as the CT (nm), the SiO_2 nanoparticle quantity (SNP) (mg·l^{-1}) and temperature (T) of the panel surface (°C) with SPE according to the following response surface equation [168]:

$$T = \Phi(s_1, s_2 \ldots s_k) \pm \text{er}. \tag{19}$$

In the above equation, the response is indicated as T. The quantitative factors are represented as s_1, s_2,..., s_k. Using this equation, the response function was developed. In equation (17), er is the residual error. A characteristic surface was developed for the independent variables to predict the output responses. With the three technological parameters (SiO_2 nanoparticle addition, CT and temperature), the objective function was set to maximize the output (SPE). The response surface was prepared with the three parameters by varying them from lower (coded value −1.68) to higher (coded value +1.68).

The developed response surface model was fitted using multiple regression equations. With circular shapes, the dependence of SiO_2 nanoparticle addition (SNP), CT and temperature (T) was traced with SPE. Three contours were developed with one process parameter as constant and two input parameters on either side. The optimal region in the contours was identified using visual inspection. Using first-order equations, simple contours can be developed. As the order increases, the complexity of the contours also increases [169].

The response surface was characterized within the range of the stationary point. The stationary point was characterized as the maximum, minimum or saddle point. Using Design Expert Software, contour plots were developed. The optimal region was identified by evaluating the shapes of the contours. Circular shapes of contours indicate that the factors are independent, and elliptical shapes of contours show that interaction occurs between the factors [170]. The contour plots for the optimization model are shown in Figure 7. Figure 7(a) shows the contour plots for CT vs SNP, Figure 7(b) shows the contour plots for CT vs T and Figure 7(c) shows the contour plots for SNP vs T. All the three contours are elliptical in shape. This indicated that interactions were present between the input process parameters. Three-dimensional surface plots were prepared by taking two of the input parameters in the mid-level and were plotted in the reference X and Y axes. The response such as the SPE was plotted on the Z-axis. The optimal point was identified from the plotted surfaces. The 3-D surface plots for the optimization model are shown in Figure 8. Figure 8(a) shows the 3-D surface plots for CT vs SNP, Figure 8(b) shows the 3-D surface plots for CT vs T and Figure 8(c) shows the 3-D surface plots for SNP vs T.

On evaluating the contours and surface plots, maximum SPE was predicted to be 17.1%. The optimized

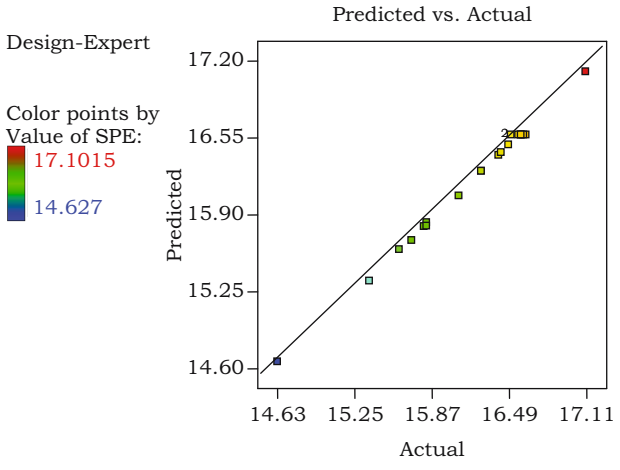

Figure 6: Relationship between the predicted and actual values of PTFE-modified silica hydrosol-coated SPE.

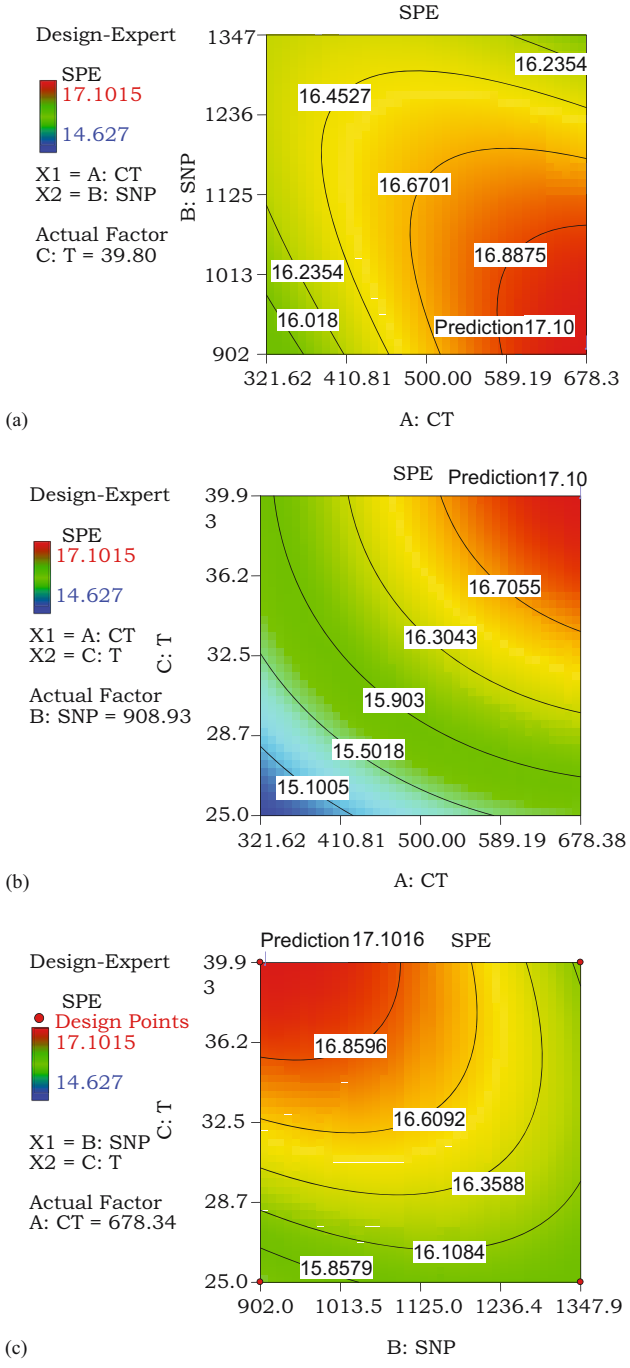

Figure 7: Contour plots of the optimization model: (a) CT vs SNP, (b) CT vs *T* and (c) SNP vs *T*.

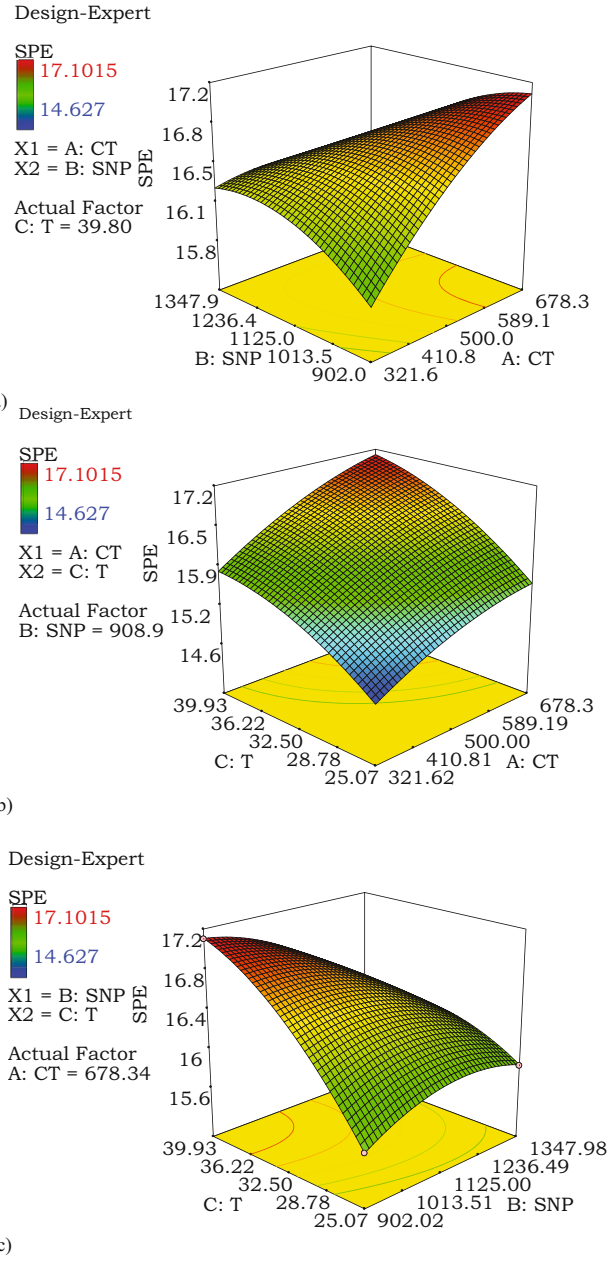

Figure 8: 3-D Surface plots of the optimization model: (a) CT vs SNP, (b) CT vs *T* and (c) SNP vs *T*.

process parameter values determined by the prediction model for achieving the efficiency were as follows: CT, 675 nm; SiO_2 nanoparticle quantity, 905 mg·l^{-1}; temperature, 40°C.

For validating the optimization model, validation experiments were conducted by using the optimized process parameter values. Using a SiO_2 quantity of 905 mg·l^{-1}, a CT of

Table 9: Validation experiments and error percentage

Exp No.	PTFE-modified silica sol-coated SPE		Error%
	Predicted	Experimental	
1	17.1%	16.98%	−0.7
2		17.04%	−0.35
3		16.83%	−1.09

675 nm and a temperature of 40°C, the output voltage, current and input solar irradiance were recorded and the output efficiency of the solar panel was calculated. Three validation experiments were conducted, and the difference between the predicted and actual efficiency was recorded. The validation results are shown in Table 9. On observing the validation results, the difference between the predicted and actual values was less than 3%, which indicated that the model was developed with very high predictability.

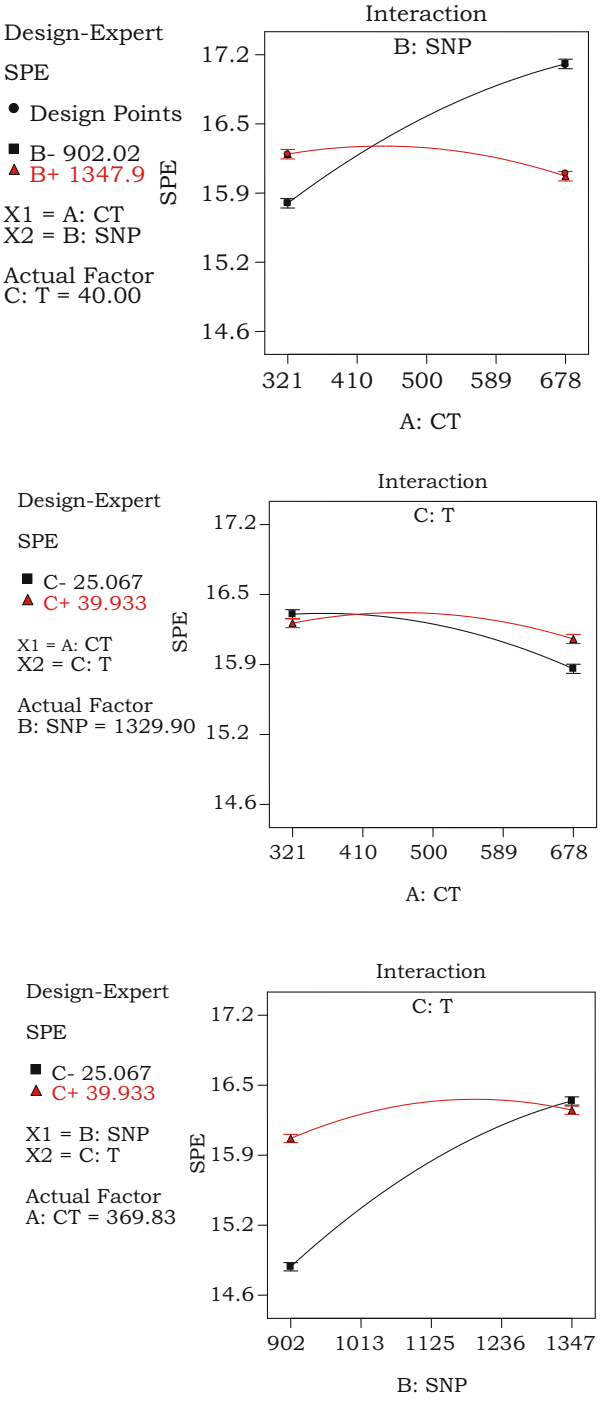

Figure 9: Interaction plots between (a) CT and SNP, (b) CT and *T*, and (c) SNP and *T*.

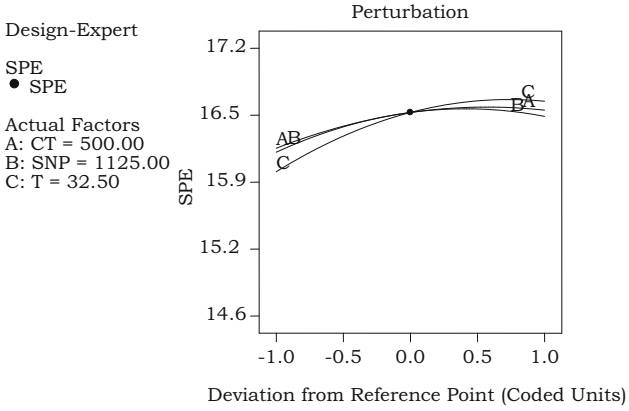

Figure 10: Perturbation plots.

3.6 Interaction and perturbation plots

For identifying the effect of variations in input technological parameters on the output responses, interaction and perturbation plots were developed. Two input technological parameters were varied while keeping the third parameter constant. The interaction plots of the solar panel model are shown in Figure 9. The interaction between SNP and CT at constant *T* of 40°C (40°C approx) is shown in Figure 9(a), and the interaction between *T* and CT at constant SNP of 1,330 mg·l^{-1} is shown in Figure 9(b). In both, interactions occurred in the lower range of the input technological parameters. The interaction between *T* and SNP at a constant CT of 370 nm is shown in Figure 9(c). In this, the interaction occurred in the upper range of the technological parameters. The perturbation plot for the solar panel model is shown in Figure 10.

Perturbation plots were plotted to find the pattern of fluctuations in SPE, on inducing variations in the technological parameters. This indicated that variations in the temperature affected SPE to a greater extent than the addition of SiO_2 nanoparticle quantity and variations in the CT.

4 Conclusions

This investigation was aimed to improve the performance and efficiency of photovoltaic solar panels. The contribution of this investigation includes the following.

i. Anti-reflective and water-repelling coating (silicon dioxide nanoparticles incorporated PTFE-modified silica hydrosols) on the solar panel to achieve higher performance in dynamic Indian environmental conditions was developed.
ii. Using a progressive, incremental MLP technique, with one hidden layer and eight nodes, a highly accurate ANN model was developed.
iii. The obtained values of performance indicators such as the MAPE, RRMSE, MBE and the coefficient of determination (R^2) indicated that (silicon dioxide nanoparticle quantity, CT, surface temperature and solar insolation) the model was better than other developed models.
iv. Feasibility limits for technological parameters were formulated, and the relationship between the input parameters and SPE was developed using the CCD model.
v. Using ANOVA, the significance of the developed model was ascertained to a confidence level greater than 95%.
vi. The input process parameters were optimized using RSM to achieve maximum SPE. Interactions and perturbation plots were developed to study the influence of the parameters on the output. The CT was found to affect the efficiency to a greater extent than other parameters. This helps in identifying parameters of primary importance, affecting SPE.
vii. This study would be useful for future engineers and researchers to identify the feasible and optimum conditions for coating, design and installation of solar panels in South Asian countries like India.

Acknowledgements: The authors thank the assistance rendered by the Advanced Thermal Engineering Laboratory, Department of Mechanical Engineering, BIT Campus, Anna University. Tiruchirappalli, Tamil Nadu, India, for conducting experiments on photovoltaic solar panels.

Funding information: No external funding was received for this research investigation.

Author contributions: Kirthika Ramasamy contributed to performing the experiments, draft preparation, investigation, conceptualization, data curation and software. Dr. Chandrasekar Murugesan contributed to the methodology, analysis and editing. Dr. Senthilkumar Thamilkolunthu contributed to the review and supervision.

Conflict of interest: The authors state that there is no conflict of interest.

Data availability statement: The authors state that the data that support the findings of this investigation are available within the manuscript.

References

[1] Bogdanov, D., A. Gulagi, M. Fasihi, and C. Breyer. Full energy sector transition towards 100% renewable energy supply: Integrating power, heat, transport and industry sectors including desalination. *Applied Energy*, Vol. 283, 2021, id. 116273.
[2] Raina, G. and S. Sinha. Outlook on the Indian scenario of solar energy strategies: Policies and challenges. *Energy Strategy Reviews*, Vol. 24, 2019, pp. 331–341.
[3] Singh, G. K. Solar power generation by PV (photovoltaic) technology: A review. *Energy*, Vol. 53, 2013, pp. 1–3.
[4] Kannan, N. and D. Vakeesan. Solar energy for future world – A review. *Renewable and Sustainable Energy Reviews*, Vol. 62, 2016, pp. 1092–1105.
[5] Sarver, T., A. Al-Qaraghuli, and L. L. Kazmerski. A comprehensive review of the impact of dust on the use of solar energy: History, investigations, results, literature, and mitigation approaches. *Renewable and Sustainable Energy Reviews*, Vol. 22, 2013, pp. 698–733.
[6] Kirpichnikova, I. M. and V. Shestakova. Problems of using solar photovoltaic panels and ways to increase their efficiency. *International Conference on Industrial Engineering, Applications and Manufacturing* (*ICIEAM*), May 18, 2020, pp. 1–7.
[7] Mohamed, A. O. and A. Hasan. Effect of dust accumulation on performance of photovoltaic solar modules in Sahara environment. *Journal of Basic and Applied Scientific Research*, Vol. 2, No. 11, 2012, pp. 11030–11036.
[8] Mozumder, M. S., A. H. Mourad, H. Pervez, and R. Surkatti. Recent developments in multifunctional coatings for solar panel applications: A review. *Solar Energy Materials and Solar Cells*, Vol. 189, 2019, pp. 75–102.
[9] Singh, C. and S. H. Kumar. *Anti-reflection and light trapping in c-Si solar cells*, Springer, India, 2018.
[10] Raut, H. K., A. S. Nair, S. S. Dinachali, V. A. Ganesh, T. M. Walsh, and S. Ramakrishna. Porous SiO_2 anti-reflective coatings on large-area substrates by electrospinning and their application to solar modules. *Solar Energy Materials and Solar Cells*, Vol. 111, 2013, pp. 9–15.
[11] Rezaei, N., O. Isabella, Z. A. Vroon, and M. Zeman. Optical optimization of a multi-layer wideband anti-reflection coating using porous MgF_2 for sub-micron-thick CIGS solar cells. *Solar Energy*, Vol. 177, 2019, pp. 59–67.
[12] Sertel, T., Y. Ozen, V. Baran, and S. Ozcelik. Effect of single-layer Ta_2O_5 and double-layer SiO_2/Ta_2O_5 anti-reflective coatings on GaInP/GaAs/Ge triple-junction solar cell

performance. *Journal of Alloys and Compounds*, Vol. 806, 2019, pp. 439–450.
[13] Jung, J., A. Jannat, M. S. Akhtar, and O. Yang. Sol–gel deposited double layer TiO_2 and Al_2O_3 anti-reflection coating for silicon solar cell. *Journal of Nanoscience and Nanotechnology*, Vol. 18, No. 2, 2018, pp. 1274–1278.
[14] Ye, T., S. Ma, X. Jiang, L. Wei, C. Vijila, and S. Ramakrishna. Performance enhancement of tri-cation and dual-anion mixed perovskite solar cells by Au@ SiO2 nanoparticles. *Advanced Functional Materials*, Vol. 27, No. 22, 2017, id. 1606545.
[15] Banerjee, D., S. S. B. Moram, C. Byram, J. Rathod, T. Jena, G. K. Podagatlapalli, et al. Plasmon-enhanced ultrafast and tunable thermo-optic nonlinear optical properties of femtosecond laser ablated TiO2 and Silver-doped TiO_2 nanoparticles. *Applied Surface Science*, Vol. 569, 2021, id. 151070.
[16] Kumar, R. and K. K. Raina. Morphological control and switchable photoluminescence responses of silica nanoparticles-modified polymer-dispersed liquid crystal composite films. *Liquid Crystals*, Vol. 42, No. 1, 2015, pp. 119–126.
[17] Kozuka, H., A. Yamano, M. Fujita, and H. Uchiyama. Aqueous dip-coating route to dense and porous silica thin films using silica nanocolloids with an aid of polyvinylpyrrolidone. *Journal Of Sol-Gel Science And Technology*, Vol. 61, 2012, pp. 381–389.
[18] Liang, Z., M. Geng, B. Dong, L. Zhao, and S. Wang. Transparent and robust SiO2/PDMS composite coatings with self-cleaning. *Surface Engineering*, Vol. 36, No. 6, 2020, pp. 643–650.
[19] Islam, M., M. R. Azhar, N. Fredj, T. D. Burleigh, O. R. Oloyede, A. A. Almajid, et al. Influence of SiO2 nanoparticles on hardness and corrosion resistance of electroless Ni–P coatings. *Surface and Coatings Technology*, Vol. 261, 2015, pp. 141–148.
[20] Shanmugam, N., R. Pugazhendhi, R. M. Elavarasan, P. Kasiviswanathan, and N. Das. Anti-reflective coating materials: a holistic review from PV perspective. *Energies*, Vol. 13, No. 10, 2020, id. 2631.
[21] Zahid, M. A., H. Park, Y. H. Cho, and J. Yi. Plasma etched PMMA/CaF_2 anti-reflection coating for light weight PV module. *Optical Materials*, Vol. 112, 2021, id. 110813.
[22] Naphade, R. A., M. Tathavadekar, J. P. Jog, S. Agarkar, and S. Ogale. Plasmonic light harvesting of dye sensitized solar cells by Au-nanoparticle loaded TiO_2 nanofibers. *Journal of Materials Chemistry A*, Vol. 2, No. 4, 2014, pp. 975–984.
[23] Aytug, T., A. R. Lupini, G. E. Jellison, P. C. Joshi, I. H. Ivanov, T. Liu, et al. Monolithic graded-refractive-index glass-based antireflective coatings: Broadband/omnidirectional light harvesting and self-cleaning characteristics. *Journal of Materials Chemistry C*, Vol. 3, No. 21, 2015, pp. 5440–5449.
[24] Kim, D. H., B. Dudem, J. W. Jung, and J. S. Yu. Boosting light harvesting in perovskite solar cells by biomimetic inverted hemispherical architectured polymer layer with high haze factor as an antireflective layer. *ACS Applied Materials & Interfaces*, Vol. 10, No. 15, 2018, pp. 13113–13123.
[25] Ye, L., Y. Zhang, X. Zhang, T. Hu, R. Ji, B. Ding, et al. Sol–gel preparation of $SiO_2/TiO_2/SiO_2$–TiO_2 broadband antireflective coating for solar cell cover glass. *Solar Energy Materials and Solar Cells*, Vol. 111, 2013, pp. 160–164.
[26] Makableh, Y. F., R. Vasan, J. C. Sarker, A. I. Nusir, S. Seal, and M. O. Manasreh. Enhancement of GaAs solar cell performance by using a ZnO sol–gel anti-reflection coating. *Solar Energy Materials and Solar Cells*, Vol. 123, 2014, pp. 178–182.
[27] Bautista, M. C. and A. Morales. Silica antireflective films on glass produced by the sol–gel method. *Solar Energy Materials and Solar Cells*, Vol. 80, No. 2, 2003, pp. 217–225.
[28] Xian, G., J. Xiong, H. Zhao, H. Fan, Z. Li, and H. Du. Evaluation of the structure and properties of the hard TiAlN-(TiAlN/CrAlSiN)-TiAlN multiple coatings deposited on different substrate materials. *International Journal of Refractory Metals and Hard Materials*, Vol. 85, 2019, id. 105056.
[29] Haynes, J. A., B. A. Pint, W. D. Porter, and I. G. Wright. Comparison of thermal expansion and oxidation behavior of various high-temperature coating materials and superalloys. *Materials at high temperatures*, Vol. 21, No. 2, 2004, pp. 87–94.
[30] Teixeira, V., M. Andritschky, W. Fischer, H. P. Buchkremer, and D. Stöver. Analysis of residual stresses in thermal barrier coatings. *Journal of Materials Processing Technology*, Vol. 92, 1999, pp. 209–216.
[31] Kloskowski, A., M. Pilarczyk, W. Chrzanowski, and J. Namieśnik. Sol-gel technique—a versatile tool for adsorbent preparation. *Critical Reviews in Analytical Chemistry*, Vol. 40, No. 3, 2010, pp. 172–186.
[32] Sun, X., X. Xu, G. Song, J. Tu, L. Li, P. Yan, et al. Preparation of MgF2/SiO2 coating with broadband antireflective coating by using sol–gel combined with electron beam evaporation. *Optical Materials*, Vol. 101, 2020, id. 109739.
[33] Foorginezhad, S. and M. M. Zerafat. Fabrication of stable fluorine-free superhydrophobic fabrics for anti-adhesion and self-cleaning properties. *Applied Surface Science*, Vol. 464, 2019, pp. 458–471.
[34] Mishra, A. K., S. Bose, T. Kuila, N. H. Kim, and J. H. Lee. Silicate-based polymer-nanocomposite membranes for polymer electrolyte membrane fuel cells. *Progress in polymer Science*, Vol. 37, No. 6, 2012, pp. 842–869.
[35] Bai, Y., H. Zhang, Y. Shao, H. Zhang, and J. Zhu. Recent progresses of superhydrophobic coatings in different application fields: An overview. *Coatings*, Vol. 11, No. 2, 2021, id. 116.
[36] Shi, Y., X. Feng, H. Wang, and X. Lu. The effect of surface modification on the friction and wear behavior of carbon nanofiber-filled PTFE composites. *Wear*, Vol. 264, No. 11–12, 2008, pp. 934–939.
[37] Jalaly, S., M. Vahdani, M. Shahabadi, and G. M. Sadeghi. Design, fabrication, and measurement of a polymer-based anti-reflection coating for improved performance of a solar panel under a specific incident angle. *Solar Energy Materials and Solar Cells*, Vol. 189, 2019, pp. 175–180.
[38] Osorio, E., R. Urteaga, L. N. Acquaroli, G. G. Salgado, H. Juarez, and R. R. Koropecki. Optimization of porous silicon multilayer as antireflection coatings for solar cells. *Solar Energy Materials and Solar Cells*, Vol. 95, No. 11, 2011, pp. 3069–3073.
[39] Rubino, F., P. Poza, G. Pasquino, and P. Carlone. Thermal spray processes in concentrating solar power technology. *Metals*, Vol. 11, No. 9, 2021, id. 1377.
[40] Adak, D., S. Ghosh, P. Chakraborty, K. M. Srivatsa, A. Mondal, H. Saha, et al. Non lithographic block copolymer directed self-assembled and plasma treated self-cleaning transparent coating for photovoltaic modules and other solar

energy devices. *Solar Energy Materials and Solar Cells*, Vol. 188, 2018, pp. 127–139.
[41] Ferrari, M. and F. Cirisano. High transmittance and highly amphiphobic coatings for environmental protection of solar panels. *Advances in Colloid and Interface Science*, Vol. 286, 2020, id. 102309.
[42] Aziz, F. and A. F. Ismail. Spray coating methods for polymer solar cells fabrication: A review. *Materials Science in Semiconductor Processing*, Vol. 39, 2015, pp. 416–425.
[43] Syafiq, A., A. K. Pandey, N. N. Adzman, and N. A. Rahim. Advances in approaches and methods for self-cleaning of solar photovoltaic panels. *Solar Energy*, Vol. 162, 2018, pp. 597–619.
[44] Huang, B. J., T. H. Lin, W. C. Hung, and F. S. Sun. Performance evaluation of solar photovoltaic/thermal systems. *Solar energy*, Vol. 70, No. 5, 2001, pp. 443–448.
[45] Kalogirou, S. and A. Sencan. Artificial intelligence techniques in solar energy applications. *Solar Collectors and Panels, Theory and Applications*, Vol. 15, 2010, pp. 315–340.
[46] Abadi, I., A. Soeprijanto, and A. Musyafa. Design of single axis solar tracking system at photovoltaic panel using fuzzy logic controller. *5th Brunei International Conference on Engineering and Technology* (*BICET 2014*), 2014, pp. 2–4.
[47] Hosoz, M. and H. M. Ertunc. Artificial neural network analysis of an automobile air conditioning system. *Energy Conversion and Management*, Vol. 47, No. 11–12, 2006, pp. 1574–1587.
[48] Kumar, G. and P. K. Mondal. Application of artificial neural network for understanding multi-layer microscale transport comprising of alternate Newtonian and non-Newtonian fluids. *Colloids and Surfaces A: Physicochemical and Engineering Aspects*, Vol. 642, 2022, id. 128664.
[49] Nespoli, A., E. Ogliari, A. Dolara, F. Grimaccia, S. Leva, and M. Mussetta. Validation of ANN training approaches for day-ahead photovoltaic forecasts. In *2018 International Joint Conference on Neural Networks* (*IJCNN*), IEEE, 2018 Jul 8, pp. 1–6.
[50] Olabi, A. G., M. Mahmoud, B. Soudan, T. Wilberforce, and M. Ramadan. Geothermal based hybrid energy systems, toward eco-friendly energy approaches. *Renewable Energy*, Vol. 147, 2020, pp. 2003–2012.
[51] Dowla, F. U., F. J. Dowla, and L. L. Rogers. *Solving problems in environmental engineering and geosciences with artificial neural networks*, Mit Press, Cambridge, Massachusetts, United States, 1995.
[52] Gandomi, A. H. and A. H. Alavi. A new multi-gene genetic programming approach to non-linear system modeling. Part II: geotechnical and earthquake engineering problems. *Neural Computing and Applications*, Vol. 1, 2012, pp. 189–201.
[53] Hema, M., D. Toghraie, and F. Amoozad. Prediction of viscosity of MWCNT-Al2O3 (20: 80)/SAE40 nano-lubricant using multi-layer artificial neural network (MLP-ANN) modeling. *Engineering Applications of Artificial Intelligence*, Vol. 121, 2023, id. 105948.
[54] Kattenborn, T., J. Leitloff, F. Schiefer, and S. Hinz. Review on convolutional neural networks (CNN) in vegetation remote sensing. *ISPRS Journal of Photogrammetry and Remote Sensing*, Vol. 173, 2021, pp. 24–49.
[55] Medsker, L. R. and L. C. Jain. Recurrent neural networks. *Design and Applications*, Vol. 5, 2001, pp. 64–67.
[56] Mohamed, A. R., G. Hinton, and G. Penn. Understanding how deep belief networks perform acoustic modelling. *IEEE International Conference on Acoustics, Speech and Signal Processing*, Vol. 1, 2012, pp. 4273–4276.
[57] Fischer, A. and C. Igel. An introduction to restricted Boltzmann machines. In *Progress in Pattern Recognition, Image Analysis, Computer Vision, and Applications: 17th Iberoamerican Congress, CIARP 2012*, Vol. 17, 2012, pp. 14–36.
[58] Theodoridis, T., V. Solachidis, N. Vretos, and P. Daras. Human fall detection from acceleration measurements using a recurrent neural network. In *Precision Medicine Powered by pHealth and Connected Health: ICBHI 2017*, Vol. 7, 2018, pp. 145–149.
[59] Avola, D., M. Bernardi, L. Cinque, G. L. Foresti, and C. Massaroni. Exploiting recurrent neural networks and leap motion controller for the recognition of sign language and semaphoric hand gestures. *IEEE Transactions on Multimedia*, Vol. 21, No. 1, 2018, pp. 234–245.
[60] Qin, C., G. Shi, J. Tao, H. Yu, Y. Jin, J. Lei, et al. Precise cutterhead torque prediction for shield tunneling machines using a novel hybrid deep neural network. *Mechanical Systems and Signal Processing*, Vol. 151, 2021, id. 107386.
[61] Liu, T., T. Wu, M. Wang, M. Fu, J. Kang, and H. Zhang. Recurrent neural networks based on LSTM for predicting geomagnetic field. In *2018 IEEE International Conference on Aerospace Electronics and Remote Sensing Technology* (*ICARES*), Vol. 1, 2018, pp. 1–5.
[62] Shi, Y., X. Song, and G. Song. Productivity prediction of a multilateral-well geothermal system based on a long short-term memory and multi-layer perceptron combinational neural network. *Applied Energy*, Vol. 282, 2021, id. 116046.
[63] Quoc Bao, T., N. T. Tan Kiet, T. Quoc Dinh, and H. X. Hiep. Plant species identification from leaf patterns using histogram of oriented gradients feature space and convolution neural networks. *Journal of Information and Telecommunication*, Vol. 4, No. 2, 2012, pp. 140–150.
[64] Meng, Y. and A. Rumshisky. Context-aware neural model for temporal information extraction. In *Proceedings of the 56th Annual Meeting of the Association for Computational Linguistics*, Vol. 1, 2018, pp. 527–536.
[65] Wang, S., R. Clark, H. Wen, and N. Trigoni. Deepvo: Towards end-to-end visual odometry with deep recurrent convolutional neural networks. In *2017 IEEE International Conference on Robotics and Automation* (*ICRA*), Vol. 1, 2017, pp. 2043–2050.
[66] Kalteh, A. M. and R. Berndtsson. Interpolating monthly precipitation by self-organizing map (SOM) and multilayer perceptron (MLP). *Hydrological Sciences Journal*, Vol. 52, No. 2, 2007, pp. 305–317.
[67] Al-Anazi, A. F. and I. D. Gates. Support vector regression for porosity prediction in a heterogeneous reservoir: A comparative study. *Computers & Geosciences*, Vol. 36, No. 12, 2010, pp. 1494–1503.
[68] Pahwa, K. and R. Kumar. R. Prediction of heart disease using hybrid technique for selecting features. In *2017 4th IEEE Uttar Pradesh section International Conference on Electrical, Computer and Electronics* (*UPCON*), Vol. 1, 2017, pp. 500–504.

[69] Stretcu, O., K. Viswanathan, D. Movshovitz-Attias, E. Platanios, S. Ravi, and A. Tomkins. Graph agreement models for semi-supervised learning. *Advances in Neural Information Processing Systems*, Vol. 32, 2019, pp. 1–11.

[70] Jin, L., Z. Wang, R. Gu, C. Yuan, and Y. Huang. Training large scale deep neural networks on the intel xeon phi many-core coprocessor. In *2014 IEEE International Parallel & Distributed Processing Symposium Workshops*, Vol. 1, 2014, pp. 1622–1630.

[71] Li, X., F. Zhao, and Y. Guo. Conditional restricted boltzmann machines for multi-label learning with incomplete labels. In *Artificial intelligence and statistics*, Proceedings of Machine Learning Research Press, Maastricht University, Netherlands, 2015, pp. 635–643.

[72] Liao, S., X. Jiang, and Z. Ge. Weakly supervised multilayer perceptron for industrial fault classification with inaccurate and incomplete labels. *IEEE Transactions on Automation Science and Engineering*, Vol. 19, No. 2, 2020, pp. 1192–1201.

[73] Sazal, M. M. R., S. K. Biswas, M. F. Amin, and K. Murase. Bangla handwritten character recognition using deep belief network. In *2013 International Conference on Electrical Information and Communication Technology*, Vol. 1, 2013, pp. 1–5.

[74] Liu, H. and B. Lang. Machine learning and deep learning methods for intrusion detection systems: A survey. *Applied Sciences*, Vol. 9, No. 20, 2019, id. 4396.

[75] Roy, P. P., G. Zhong, and M. Cheriet. Tandem hidden Markov models using deep belief networks for offline handwriting recognition. *Frontiers of Information Technology & Electronic Engineering*, Vol. 18, No. 7, 2017, pp. 978–988.

[76] Hanggara, F. S., and K. Anam. Sequence-based protein-protein interaction prediction using greedy layer-wise training of deep neural networks. In *AIP Conference Proceedings*, Vol. 2278, No. 1, 2020, p. 020050.

[77] Moghaddamnia, A., R. Remesan, M. H. Kashani, M. Mohammadi, D. Han, and J. Piri. Comparison of LLR, MLP, Elman, NNARX and ANFIS Models—with a case study in solar radiation estimation. *Journal of Atmospheric and Solar-Terrestrial Physics*, Vol. 71, No. 8–9, 2009, pp. 975–982.

[78] Hong, H., Z. Zhang, A. Guo, L. Shen, H. Sun, Y. Liang, et al. Radial basis function artificial neural network (RBF ANN) as well as the hybrid method of RBF ANN and grey relational analysis able to well predict trihalomethanes levels in tap water. *Journal of Hydrology*, Vol. 591, 2020, id. 125574.

[79] Xia, Y., H. Leung, and J. Wang. A projection neural network and its application to constrained optimization problems. *IEEE Transactions on Circuits and Systems I: Fundamental Theory and Applications*, Vol. 49, No. 4, 2002, pp. 447–458.

[80] Aydin, O. and S. Guldamlasioglu. Using LSTM networks to predict engine condition on large scale data processing framework. In *2017 4th International Conference on Electrical and Electronic Engineering* (*ICEEE*), Vol. 1, 2017, pp. 281–285.

[81] Hammerstrom, D. Working with neural networks. *IEEE Spectrum*, Vol. 30, No. 7, 1993, pp. 46–53.

[82] Rezaeian Zadeh, M., S. Amin, D. Khalili, and V. P. Singh. Daily outflow prediction by multi layer perceptron with logistic sigmoid and tangent sigmoid activation functions. *Water Resources Management*, Vol. 24, 2010, pp. 2673–2688.

[83] Zhang, H., Y. Wang, and C. Deng. August. Application of gesture recognition based on simulated annealing BP neural network. In *Proceedings of 2011 International Conference on Electronic & Mechanical Engineering and Information Technology*, Vol. 1, 2011, pp. 178–181.

[84] Wu, Y., M. Yuan, S. Dong, L. Lin, and Y. Liu. Remaining useful life estimation of engineered systems using vanilla LSTM neural networks. *Neurocomputing*, Vol. 275, 2018, pp. 167–179.

[85] Chandwani, V., V. Agrawal, and R. Nagar. Modeling slump of ready mix concrete using genetic algorithms assisted training of Artificial Neural Networks. *Expert Systems with Applications*, Vol. 42, No. 2, 2015, pp. 885–893.

[86] Blanco, M., J. Coello, H. Iturriaga, S. Maspoch, and J. Pages. NIR calibration in non-linear systems: different PLS approaches and artificial neural networks. *Chemometrics and Intelligent Laboratory Systems*, Vol. 50, No. 1, 2000, pp. 75–82.

[87] Raissi, S. and R. E. Farsani. Statistical process optimization through multi-response surface methodology. *World Academy of Science, Engineering and Technology*, Vol. 51, No. 46, 2009, pp. 267–271.

[88] Khayet, M. and C. Cojocaru. Air gap membrane distillation: Desalination, modeling and optimization. *Desalination*, Vol. 287, 2012, pp. 138–145.

[89] Pongcharoen, P., W. Chainate, and P. Thapatsuwan. Exploration of genetic parameters and operators through travelling salesman problem. *Science Asia*, Vol. 33, No. 2, 2007, pp. 215–222.

[90] Quaid, M. A. K. and A. Jalal. Wearable sensors based human behavioral pattern recognition using statistical features and reweighted genetic algorithm. *Multimedia Tools and Applications*, Vol. 79, 2020, pp. 6061–6083.

[91] Kaur, G. and J. S. Dhillon. Economic power generation scheduling exploiting hill-climbed Sine–Cosine algorithm. *Applied Soft Computing*, Vol. 111, 2021, id. 107690.

[92] Afzalinia, A., M. Mirzaee, and M. A. Amani. Design of an S-scheme photo-catalyst utilizing a Cu-doped perovskite and MOF-5 for simultaneous degradation of organic pollutants under LED light irradiation: Application of EXRSM method for spectra separation and BBD-RSM modeling. *Spectrochimica Acta Part A: Molecular and Biomolecular Spectroscopy*, Vol. 287, 2023, id. 122116.

[93] Guan, B., M. Wan, X. Wu, X. Cui, and B. Zhou. Non-probabilistic optimization model of engineering structures with dependent interval variables. *Applied Mathematical Modelling*, Vol. 102, 2022, pp. 285–304.

[94] Saxena, V., N. Kumar, and V. K. Saxena. RSM/DFA computation approach for optimization and modeling of CI engine performance and emission characteristics fuelled with preheated fuel blend modified withTiO2 nanomaterial. *Materials Today: Proceedings*, Vol. 38, 2021, pp. 350–358.

[95] Liang, C., Y. Rao, J. Luo, and X. Luo. Experimental and numerical study of turbulent flow and heat transfer in a wedge-Shaped Channel with guiding pin fins for turbine blade trailing edge cooling. *International Journal of Heat and Mass Transfer*, Vol. 178, 2021, id. 121590.

[96] Makhlouf, A., A. Belaadi, M. Boumaaza, L. Mansouri, M. Bourchak, and M. Jawaid. Water absorption behavior of jute fibers reinforced HDPE biocomposites: Prediction using

RSM and ANN modeling. *Journal of Natural Fibers*, Vol. 19, No. 16, 2022, pp. 14014–14031.
[97] Breig, S. J. M. and K. J. K. Luti. Response surface methodology: A review on its applications and challenges in microbial cultures. *Materials Today: Proceedings*, Vol. 42, 2021, pp. 2277–2284.
[98] Chananipoor, A., Z. Azizi, B. Raei, and N. Tahmasebi. Optimization of the thermal performance of nano-encapsulated phase change material slurry in double pipe heat exchanger: Design of experiments using response surface methodology (RSM). *Journal of Building Engineering*, Vol. 34, 2021, id. 101929.
[99] Bashiri, M. and A. F. Geranmayeh. Tuning the parameters of an artificial neural network using central composite design and genetic algorithm. *Scientia Iranica*, Vol. 18, No. 6, 2011, pp. 1600–1608.
[100] Ferreira, S. C., R. E. Bruns, H. S. Ferreira, G. D. Matos, J. M. David, G. C. Brandao, et al. Box-Behnken design: an alternative for the optimization of analytical methods. *Analytica chimica acta*, Vol. 597, No. 2, 2007, pp. 179–186.
[101] Pabari, R. M. and Z. Ramtoola. Application of face centred central composite design to optimise compression force and tablet diameter for the formulation of mechanically strong and fast disintegrating orodispersible tablets. *International Journal of Pharmaceutics*, Vol. 430, No. 1–2, 2012, pp. 18–25.
[102] Cavalcante, K. S., M. N. Penha, K. K. Mendonca, H. C. Louzeiro, A. C. Vasconcelos, A. P. Maciel, et al. Optimization of transesterification of castor oil with ethanol using a central composite rotatable design (CCRD). *Fuel*, Vol. 89, No. 5, 2010, pp. 1172–1176.
[103] Iversen, G. R., H. Norpoth, and H. P. Norpoth. *Analysis of variance*, Sage, New York, United States, 1987.
[104] Okudera, H. and A. Hozumi. The formation and growth mechanisms of silica thin film and spherical particles through the Stöber process. *Thin Solid Films*, Vol. 434, No. 1–2, 2003, pp. 62–68.
[105] Basu, B. J. and V. D. Kumar. Fabrication of superhydrophobic nanocomposite coatings using polytetrafluoroethylene and silica nanoparticles. *International Scholarly Research Notices*, Vol. 2011, 2011, pp. 1–6.
[106] Hoshikawa, Y., H. Yabe, A. Nomura, T. Yamaki, A. Shimojima, and T. Okubo. Mesoporous silica nanoparticles with remarkable stability and dispersibility for antireflective coatings. *Chemistry of Materials*, Vol. 22, No. 1, 2010, pp. 12–14.
[107] Poorebrahimi, S. and R. Norouzbeigi. A facile solution-immersion process for the fabrication of superhydrophobic gibbsite films with a binary micro-nano structure: effective factors optimization via Taguchi method. *Applied Surface Science*, Vol. 356, 2015, pp. 157–166.
[108] Mostaghimi, J., S. Chandra, R. G. Azar, and A. Dolatabadi. Modeling thermal spray coating processes: a powerful tool in design and optimization. *Surface and Coatings Technology*, Vol. 163, 2003 Jan 30, id. 1.
[109] Rizwan, M., M. Jamil, S. Kirmani, and D. P. Kothari. Fuzzy logic based modeling and estimation of global solar energy using meteorological parameters. *Energy*, Vol. 70, 2014, pp. 685–691.
[110] Galiano, V. R., M. S. Castillo, M. C. Olmo, and M. J. C. Rivas. Machine learning predictive models for mineral prospectivity: An evaluation of neural networks, random forest, regression trees and support vector machines. *Ore Geology Reviews*, Vol. 71, 2015, pp. 804–818.
[111] Vujicic, T., T. Matijevic, J. Ljucovic, A. Balota, and Z. Sevarac. Comparative analysis of methods for determining number of hidden neurons in artificial neural network. In *Central European Conference on Information and Intelligent Systems*, 2016, p. 219. Faculty of Organization and Informatics Varazdin.
[112] Indera, N. I., I. M. Yassin, A. Zabidi, and Z. I. Rizman. Non-linear autoregressive with exogeneous input (NARX) Bitcoin price prediction model using PSO-optimized parameters and moving average technical indicators. *Journal of Fundamental and Applied Sciences*, Vol. 9, No. art 3S, 2017, pp. 791–808.
[113] Kneller, D. G., F. E. Cohen, and R. Langridge. Improvements in protein secondary structure prediction by an enhanced neural network. *Journal of Molecular Biology*, Vol. 214, No. 1, 1990, pp. 171–182.
[114] Nawi, N. M., M. Z. Rehman, M. A. Aziz, T. Herawan, and J. H. Abawajy. An accelerated particle swarm optimization based Levenberg Marquardt back propagation algorithm. In *International Conference on Neural Information Processing*, Springer, Cham, 2014 Nov 3, pp. 245–253.
[115] Gorjian, S., T. T. Hashjin, and M. H. Khoshtaghaza. Designing and optimizing a back propagation neural network to model a thin-layer drying process. *International Agrophysics*, Vol. 25, No. 1, 2011, id. 1.
[116] Bhavsar, H. and A. Ganatra. A comparative study of training algorithms for supervised machine learning. *International Journal of Soft Computing and Engineering*, Vol. 2, No. 4, 2012, pp. 2231–2307.
[117] Zamanlooy, B. and M. Mirhassani. Efficient VLSI implementation of neural networks with hyperbolic tangent activation function. *IEEE Transactions on Very Large Scale Integration (VLSI) Systems*, Vol. 22, No. 1, 2013, pp. 39–48.
[118] Nwankpa, C., W. Ijomah, A. Gachagan, and S. Marshall. *Activation functions: Comparison of trends in practice and research for deep learning*. arXiv, 2018, preprint, arXiv:1811.03378.
[119] Al-Maqaleh, B. M., A. A. Al-Mansoub, and F. N. Al-Badani. Forecasting using artificial neural network and statistics models. *International Journal Education and Management Engineering*, Vol. 3, 2016, pp. 20–32.
[120] Myttenaere, A. D., B. Golden, B. L. Grand, and F. Rossi. Mean absolute percentage error for regression models. *Neurocomputing*, Vol. 192, 2017, pp. 38–48.
[121] Adamowski, J., H. F. Chan, S. O. Prasher, B. O. Zielinski, and A. Sliusarieva. Comparison of multiple linear and nonlinear regression, autoregressive integrated moving average, artificial neural network, and wavelet artificial neural network methods for urban water demand forecasting in Montreal, Canada. *Water Resources Research*, Vol. 48, No. 1, 2012, id. 1.
[122] Sedaghat, M. and A. Kiomarsiyan. Applying MLP-ANN as a novel and accurate method to estimate gas density. *Petroleum Science and Technology*, Vol. 37, No. 20, 2019, pp. 2128–2133.
[123] Jahani, B. and B. Mohammadi. A comparison between the application of empirical and ANN methods for estimation of daily global solar radiation in Iran. *Theoretical and Applied Climatology*, Vol. 137, No. 1, 2019, pp. 1257–1269.

[124] Chiteka, K. and C. C. Enweremadu. Prediction of global horizontal solar irradiance in Zimbabwe using artificial neural networks. *Journal of Cleaner Production*, Vol. 135, 2016, pp. 701–711.
[125] Olawoyin, A. and Y. Chen. Predicting the future with artificial neural network. *Procedia Computer Science*, Vol. 140, 2018, pp. 383–392.
[126] Davis, J. C. and R. J. Sampson. *Statistics and data analysis in geology*, Wiley, New York, 1986 Jan 17.
[127] Thinsungnoena, T., N. Kaoungkub, P. Durongdumronchaib, K. Kerdprasopb, and N. Kerdprasopb. The clustering validity with silhouette and sum of squared errors. *Learning*, Vol. 3, No. 7, 2015, id. 1.
[128] Menard, S. Coefficients of determination for multiple logistic regression analysis. *The American Statistician*, Vol. 54, No. 1, 2000, pp. 17–24.
[129] Willmott, C. J. and K. Matsuura. Advantages of the mean absolute error (MAE) over the root mean square error (RMSE) in assessing average model performance. *Climate Research*, Vol. 30, No. 1, 2005, pp. 79–82.
[130] Jiang, Y. Estimation of monthly mean daily diffuse radiation in China. *Applied Energy*, Vol. 86, No. 9, 2009, pp. 1458–1464.
[131] Bouselham, L., M. Hajji, B. Hajji, and H. Bouali. A new MPPT-based ANN for photovoltaic system under partial shading conditions. *Energy Procedia*, Vol. 111, 2017, pp. 924–933.
[132] Bandyopadhyay, G. and S. Chattopadhyay. Single hidden layer artificial neural network models versus multiple linear regression model in forecasting the time series of total ozone. *International Journal of Environmental Science & Technology*, Vol. 4, No. 1, 2007, pp. 141–149.
[133] Kim, T. and T. Adal. Approximation by fully complex multilayer perceptrons. *Neural Computation*, Vol. 15, No. 7, 2003, pp. 1641–1666.
[134] Iwundu, M. P. Optimal partially replicated cube, star and center runs in face-centered central composite designs. *International Journal of Statistics and Probability*, Vol. 4, No. 4, 2015, pp. 1–9.
[135] Siddharth, S. and T. Senthilkumar. Optimization of friction stir spot welding process parameters of dissimilar Al 5083 and C 10100 joints using response surface methodology. *Russian Journal of Non-Ferrous Metals*, Vol. 57, No. 5, 2016, pp. 456–466.
[136] Kumar, R., A. Sahoo, K. Satyanarayana, and G. Rao. Some studies on cutting force and temperature in machining Ti-6Al-4V alloy using regression analysis and ANOVA. *International Journal of Industrial Engineering Computations*, Vol. 4, No. 3, 2013, pp. 427–436.
[137] Khuri, A. I. and S. Mukhopadhyay. Response surface methodology. *Wiley Interdisciplinary Reviews: Computational Statistics*, Vol. 2, No. 2, 2010, pp. 128–149.
[138] Theppaya, T. and S. Prasertsan. Optimization of rubber wood drying by response surface method and multiple contour plots. *Drying Technology*, Vol. 22, No. 7, 2004, pp. 1637–1660.
[139] Bas, D. and I. H. Boyac. Modeling and optimization I: Usability of response surface methodology. *Journal of Food Engineering*, Vol. 78, No. 3, 2007, pp. 836–845.
[140] Abid, S., R. Messadi, T. Hassine, H. B. Daly, J. Soulestin, and M. F. Lacrampe. Optimization of mechanical properties of printed acrylonitrile butadiene styrene using RSM design. *The International Journal of Advanced Manufacturing Technology*, Vol. 100, No. 5, 2019, pp. 1363–1372.
[141] Srinivasan, R., T. Pridhar, L. S. Ramprasath, N. S. Charan, and W. Ruban. Prediction of tensile strength in FDM printed ABS parts using response surface methodology (RSM). *Materials Today: Proceedings*, Vol. 27, 2020, pp. 1827–1832.
[142] Puah, B. K., L. W. Chong, Y. W. Wong, K. M. Begam, N. Khan, M. A. Juman, et al. A regression unsupervised incremental learning algorithm for solar irradiance prediction. *Renewable Energy*, Vol. 164, 2021, pp. 908–925.
[143] Dawson, C. W. and R. Wilby. An artificial neural network approach to rainfall-runoff modelling. *Hydrological Sciences Journal*, Vol. 43, No. 1, 1998, pp. 47–66.
[144] Hoang, A. T., S. Nizetic, H. C. Ong, W. Tarelko, T. H. Le, M. Q. Chau, et al. A review on application of artificial neural network (ANN) for performance and emission characteristics of diesel engine fueled with biodiesel-based fuels. *Sustainable Energy Technologies and Assessments*, Vol. 47, 2021, id. 101416.
[145] Yang, T., A. A. Asanjan, M. Faridzad, N. Hayatbini, X. Gao, and S. Sorooshian. An enhanced artificial neural network with a shuffled complex evolutionary global optimization with principal component analysis. *Information Sciences*, Vol. 418, 2017, pp. 302–316.
[146] Sohani, A., H. Sayyaadi, H. H. Balyani, and S. Hoseinpoori. A novel approach using predictive models for performance analysis of desiccant enhanced evaporative cooling systems. *Applied Thermal Engineering*, Vol. 107, 2016, pp. 227–252.
[147] Khatib, T., A. Mohamed, M. Mahmoud, and K. Sopian. Estimating global solar energy using multilayer perception artificial neural network. *International Journal of Energy*, Vol. 6, No. 1, pp. 82–87.
[148] Salima, G. and G. M. Chavula. Determining Angstrom constants for estimating solar radiation in Malawi. *International Journal of Geosciences*, Vol. 3, No. 2, 2012, pp. 391–397.
[149] Assi, A. H., M. H. Al-Shamisi, H. A. Hejase, and A. Haddad. Prediction of global solar radiation in UAE using artificial neural networks. In *2013 International Conference on Renewable Energy Research and Applications* (*ICRERA*), IEEE, 2013 Oct 20, pp. 196–200.
[150] Yacef, R., A. Mellit, S. Belaid, and Z. Şen. New combined models for estimating daily global solar radiation from measured air temperature in semi-arid climates: application in Ghardaïa, Algeria. *Energy Conversion and Management*, Vol. 79, 2014, pp. 606–615.
[151] El-Sebaii, A. A., F. S. Al-Hazmi, A. A. Al-Ghamdi, and S. J. Yaghmour. Global, direct and diffuse solar radiation on horizontal and tilted surfaces in Jeddah, Saudi Arabia. *Applied Energy*, Vol. 87, No. 2, 2010, pp. 568–576.
[152] Poudyal, K. N., B. K. Bhattarai, B. Sapkota, and B. Kjeldstad. Estimation of global solar radiation using sunshine duration in Himalaya Region. *Research Journal of Chemical Sciences*, Vol. 2, No. 11, 2012, pp. 20–25.
[153] Tuomiranta, A., P. Marpu, S. Munawwar, and H. Ghedira. Validation of thermal models for photovoltaic cells under hot desert climates. *Energy Procedia*, Vol. 57, 2014, pp. 136–143.
[154] Bimenyimana, S., G. N. Asemota, and L. Lingling. Output power prediction of photovoltaic module using nonlinear autoregressive neural network. *Power*, Vol. 31, 2014, id. 12.

[155] Yaniktepe, B. and Y. A. Genc. Establishing new model for predicting the global solar radiation on horizontal surface. *International Journal of Hydrogen Energy*, Vol. 40, No. 44, 2015, pp. 15278–15283.

[156] Kumar, S. and T. Kaur. Development of ANN based model for solar potential assessment using various meteorological parameters. *Energy Procedia*, Vol. 90, 2016, pp. 587–592.

[157] Fukumoto, M., H. Terada, M. Mashiko, K. Sato, M. Yamada, and E. Yamaguchi. Deposition of copper fine particle by cold spray process. *Materials transactions*, Vol. 1, 2009, id. 0904200749.

[158] Raut, H. K., V. A. Ganesh, A. S. Nair, and S. Ramakrishna. Anti-reflective coatings: A critical, in-depth review. *Energy & Environmental Science*, Vol. 4, No. 10, 2011, pp. 3779–3804.

[159] Moon, J., T. K. Kim, B. VanSaders, C. Choi, Z. Liu, S. Jin, et al. Black oxide nanoparticles as durable solar absorbing material for high-temperature concentrating solar power system. *Solar Energy Materials and Solar Cells*, Vol. 134, 2015, pp. 417–424.

[160] Kolen'ko, Y. V., V. D. Maximov, A. V. Garshev, P. E. Meskin, N. N. Oleynikov, and B. R. Churagulov. Hydrothermal synthesis of nanocrystalline and mesoporous titania from aqueous complex titanyl oxalate acid solutions. *Chemical physics letters*, Vol. 388, No. 4–6, 2004, pp. 411–415.

[161] Wang, C., W. Cheng, P. Ma, R. Xia, and X. Ling. High performance Al–AlN solar spectrally selective coatings with a self-assembled nanostructure AlN anti-reflective layer. *Journal of Materials Chemistry A*, Vol. 5, No. 6, 2017, pp. 2852–2860.

[162] Montgomery, D. C. *Design and analysis of experiments*, John Wiley & Sons, New Jersey, United States, 2017.

[163] Paventhan, R., P. R. Lakshminarayanan, and V. Balasubramanian. Prediction and optimization of friction welding parameters for joining aluminium alloy and stainless steel. *Transactions of Nonferrous Metals Society of China*, Vol. 21, No. 7, 2011, pp. 1480–1485.

[164] Siddharth, S., T. Senthilkumar, and M. Chandrasekar. Development of processing windows for friction stir spot welding of aluminium Al5052/copper C27200 dissimilar materials. *Transactions of Nonferrous Metals Society of China*, Vol. 27, No. 6, 2017, pp. 1273–1284.

[165] Schielzeth, H. Simple means to improve the interpretability of regression coefficients. *Methods in Ecology and Evolution*, Vol. 1, No. 2, 2010, pp. 103–113.

[166] Cule, E., P. Vineis, and M. D. Iorio. Significance testing in ridge regression for genetic data. *BMC Bioinformatics*, Vol. 12, No. 1, 2011, pp. 1–5.

[167] Nagappan, N. and T. Ball. Use of relative code churn measures to predict system defect density. In *Proceedings of the 27th International Conference on Software Engineering*, 2005 May 15, pp. 284–292.

[168] Sumic, Z., A. Vakula, A. Tepic, J. Cakarevic, J. Vitas, and B. Pavlic. Modeling and optimization of red currants vacuum drying process by response surface methodology (RSM). *Food Chemistry*, Vol. 203, 2016, pp. 465–475.

[169] Dritschel, D. G. Contour dynamics and contour surgery: numerical algorithms for extended, high-resolution modelling of vortex dynamics in two-dimensional, inviscid, incompressible flows. *Computer Physics Reports*, Vol. 10, No. 3, 1989, pp. 77–146.

[170] Loffler, G. Perception of contours and shapes: Low and intermediate stage mechanisms. *Vision Research*, Vol. 48, No. 20, 2008, pp. 2106–2127.